Robust Bayesian calibration of a $\mathrm{k}-\epsilon$ model for compressible jet-in-crossflow simulations

Jaideep Ray*
Sandia National Laboratories, Livermore, CA 94550-0969,USA

Lawrence Dechant† and Sophia Lefantzi‡
Sandia National Laboratories, Albuquerque, NM 87185-5800, USA

Julia Ling§
Citrine Informatics, Redwood City, CA 94063, USA

Srinivasan Arunajatesan¶
Sandia National Laboratories, Albuquerque, NM 87185-5800, USA

Compressible jet-in-crossflow interactions are difficult to simulate accurately using Reynolds-averaged Navier Stokes (RANS) models. This could be due to simplifications inherent in RANS or the use of inappropriate RANS constants estimated by fitting to experiments of simple or canonical flows. Our previous work on Bayesian calibration of a $\mathrm{k}-\epsilon$ model to experimental data had led to a weak hypothesis that inaccurate simulations could be due to inappropriate constants more than model-form inadequacies of RANS. In this work, we perform Bayesian calibration of $\mathrm{k}-\epsilon$ constants to a set of experiments that span a range of Mach numbers and jet strengths. We check the variation of the calibrated constants to assess the degree to which parametric estimates compensate for RANS's model-form errors. We also develop an analytical model of jet-in-crossflow interactions and obtain estimates of $\mathrm{k}-\epsilon$ constants that are free of any conflation of parametric and RANS's model-form uncertainties. We find that the analytical $\mathrm{k}-\epsilon$ constants provide mean-flow predictions which are similar to those provided by the calibrated constants. Further, both of them provide predictions that are far closer to experimental measurements than those computed using "nominal" values of these constants simply obtained from literature. We conclude that the lack of predictive skill of RANS jet-in-crossflow simulations is mostly due to parametric inadequacies and our analytical estimates may provide a simple way of obtaining predictive compressible jet-in-crossflow simulations.

*Technical Staff, Extreme Scale Data Science and Analytics, MS 9152, Senior Member
†Technical Staff, Aerosciences Department, MS 0825, Senior Member
‡Manager, Fluid and Reactive Processes, MS 0828, Senior Member
§Manager, Data Science
¶Manager, Aerosciences Department, MS 0825, Senior Member

Nomenclature

$\mathbf{C}$	=	Parameters in the $k-\epsilon$ RANS model to be calibrated
$\mathbf{C}_a$	=	Analytical estimate of $\mathbf{C}$
$\mathbf{C}_{nom}$	=	Nominal values of $\mathbf{C}$
$\mathbf{C}_{opt}$	=	Optimal value of $\mathbf{C}$
CVP	=	Counter-rotating Vortex Pair
C_μ	=	A parameter in the eddy-viscosity sub-model in a $k-\epsilon$ RANS model
$C_{\epsilon 2}, C_{\epsilon 1}$	=	Parameters in the equation of the evolution of ϵ in a $k-\epsilon$ RANS model
d	=	Approximation error in the surrogate model
J	=	Jet-to-crossflow momentum ratio
JPDF	=	Joint probability density function
$l(x)$	=	Jet length-scale at streamwise location x
M	=	Cross-flow Mach number
$\mathcal{N}(\mu, \sigma^2)$	=	Normal distribution with mean μ and standard deviation σ
TD	=	Training Data
u_{def}	=	Velocity deficit in the streamwise direction
v_{norm}	=	Normalized vertical velocity
$f(\xi), g(\xi), h(\xi)$	=	Normalized radial profiles for streamwise velocity, turbulent kinetic energy and dissipation
x	=	streamwise distance
δ_m	=	Structural error; difference between experimental data and calibrated surrogate model predictions
σ	=	Model-data mismatch is represented as $\mathcal{N}(0, \sigma^2)$
ξ	=	Normalized radial distance, $r/l(x)$

I. Introduction

Turbulent jet-in-crossflow (JIC) interactions occur in many natural and engineering situations [1]. One such occurence, in aerodynamics, is the stabilization of aerodynamic bodies using spin rockets mounted perpendicular to the direction of flight. Here the interaction of the rocket exhaust with the freestream constitutes a JIC interaction. It is known that the exhaust can interact with the control surfaces of the aerodynamic body, modifying the pressure distribution and interfering with the moments experienced by the body [2]. Experimental investigations of the JIC interactions [3–6] show that the exhaust (the jet) rolls into a counter-rotating vortex pair (CVP), which then interacts with the fin/control surface [7]; a vortex-dynamical model of this interaction has also been proposed. However, numerical simulations using $k-\epsilon$ and $k-\omega$ RANS models could only reproduce the experimental measurements

qualitatively [8].

The lack of predictive skill of the RANS simulations could be due to two causes. First, RANS models contain constants whose values are estimated by fitting to experimental data gathered from simple flows. These flows have little in common with JIC interactions. Further, RANS parameters are often tuned for different classes of flows; see Ref. [9] for a discussion. Secondly, two-equation RANS models contain gross simplifications of turbulent processes [10], giving rise to model-form errors. It is unclear which of the two causes contributes more to the inaccuracies in JIC simulations. In one of our previous papers [9], we investigated the first possible cause of errors, i.e., whether JIC simulations could be improved by using better RANS parameters. We developed a Bayesian technique for calibrating three $k-\epsilon$ constants $\mathbf{C} = (C_\mu, C_{\epsilon 2}, C_{\epsilon 1})$ and computed a joint probability density function (JPDF) for them by calibrating to data from one of the experiments described in Refs. [3–5]. In that study, the $k-\epsilon$ RANS model employed a linear eddy viscosity model. The experiment in question consisted of a M = 3.93 jet exhausting into a M = 0.8 crossflow, providing a jet-to-crossflow momentum ratio of $J = 10.2$. We found the calibrated JPDF to be far more predictive than the nominal value of the parameters ($\mathbf{C}_{nom} = \{0.09, 1.92, 1.44\}$, taken from literature) for some of the other experiments described in Refs [3, 5]. This suggested that, perhaps, inappropriate parameters were the main cause of the large numerical inaccuracies.

As a check, in our next paper [11], we investigated the second potential cause of errors i.e., the simplifications inherent in $k-\epsilon$ RANS. We estimated a nonlinear eddy viscosity model (i.e., we inferred the model form and associated parameters) using data from the same experiment referred to above. Since this process involved discovering both model form *and* parameters for the $k-\epsilon$ RANS model, we expected that it would be substantially more predictive than our work with the linear eddy viscosity model [9]; instead, we found that their predictive skills to be quite similar. This seemed to imply that one of the most important drawback of $k-\epsilon$ RANS with linear eddy viscosity models – their inability to accommodate anisotropy in Reynolds stresses – was not as large a contributing factor to the inaccuracies in the simulated mean flows compared to inappropriate $k-\epsilon$ constants. Note that this is a weak conclusion - the model form that we learned could have been deficient due to a lack of experimental data.

These two studies seemed to indicate that parametric uncertainties, rather than model-form errors, were the primary cause of inaccuracies in JIC simulations. However, since both the investigations involved calibration (fitting to data), there was a possibility that the calibrated JPDF could be compensating for model-form errors. While the predictive skill of the JPDF for experiments not used in the calibration seemed to suggest that the degree of compensation was not large, it was hardly conclusive; the JPDF was not sharp and the estimate of $\mathbf{C}$ had a significant degree of uncertainty. In our current study, we investigate whether it may be possible to find a new value of $\mathbf{C}$ that would be predictive for JIC simulations over a range of crossflow Mach numbers M and jet-to-crossflow momentum ratios J. This implies that the model-form errors are small over a (M, J) range. It also provides an indirect check on our previous (weak) conclusion that failure to model anisotropy in turbulent stresses was a smaller source of prediction errors vis-à-vis the

use of inappropriate parameters. We will develop and compare JPDFs for the experiments in Refs. [3–5]. We do not expect the JPDFs to be identical, since the model-form errors will be different in each case. However, any points of similarity between the JPDFs would provide strong evidence of how $\mathbf{C}_{nom}$ should change in order to be predictive. We then develop an *analytical* model of JIC interactions, and obtain an estimate for $\mathbf{C}$, which we refer to as $\mathbf{C}_a$. While the analytical model involves its own set of simplifications, it does not involve fitting to experimental data, and is thus free of any conflation and compensation of parametric versus model-form uncertainties. We compare the predictive skill of $\mathbf{C}_a$ versus the calibrated JPDFs, and decide whether it might serve as an alternative to $\mathbf{C}_{nom}$.

This paper is an extension of two of our conference papers [12, 13] which contain many of the details, including the derivations. We will make references to these details in the paper, which is structured as follows. In Sec. II, we review literature on studies that seek to improve the predictive skill of RANS models by using observational data. We also review previous attempts at modeling JIC interactions analytically, and evidence from other researchers that values of $\mathbf{C}$ other than $\mathbf{C}_{nom}$ might be predictive for JIC interactions. In Sec. III, we describe the inverse modeling methodology used to compute the JPDFs from experimental data. In Sec. IV, we develop the analytical model. In Sec. V we present and discuss our results. In Sec. VI, we present our conclusions.

II. Background

A. Analytical models of JIC interactions

There have been many analytical modeling studies of JIC interactions; a comprehensive review can be found in Ref. [14]. The jet, emanating into the crossflow, bends and is swept downstream, rolling into a counter-rotating vortex pair (CVP). The bulk of the studies have targeted modeling the trajectory/penetration of the jet in the crossflow, as a function of the downstream distance. Broadwell and Breidenthal [15] derived a model that showed that in the far-field e.g., about 50 jet diameters d_j from the exit, the trajectory scaled as $y \sim x^{1/3}$, a result that agreed with incompressible experiments. They also showed that the circulation Γ of the CVP decayed downstream as $\Gamma \sim x^{-1/3}$. Karagozian [16] developed a vortex dynamical model of the CVP and rederived the same result. Her model included "viscous" vortices i.e., regions with vorticity distributed in space as a Gaussian and which spread in time due to viscous processes. She showed that Reynolds number had a weak effect on the trajectory. The model was later extended to compressible crossflows [17] using inviscid point vortices.

Hasselbrink and Mungal [14] developed scaling laws for the velocities and trajectory of the jet in JIC interactions. They divided the interaction into 3 phases. The first, called the *potential core*, extended a few d_j downstream of the exit and resembled an axisymmetric mixing layer. The second, called the *near-field*, resembled the far-field of a free jet. The trajectory scales as $y \sim x^{1/2}$. The third, called the *far-field* (about $50d_j$ downstream of the exit) displayed scalings that were reminiscent of a wake. The trajectory scales as $y \sim x^{1/3}$ and the circulation of the CVP obeys $\Gamma \sim J^{1/3}x^{-1/3}$.

The modeling efforts described above started from first principles rather than the $k-\epsilon$ model and are thus not couched in terms of $(C_\mu, C_{\epsilon 2}, C_{\epsilon 1})$. However, in one of our conference papers [13], we derived an analytical model for JIC interactions that drew on the $k-\epsilon$ model and the near-field/far-field formalism described in Ref. [14]. The scalings described above i.e., $y \sim x^{1/2}, y \sim x^{1/3}$ and $\Gamma \sim J^{1/3}x^{-1/3}$ for the near- and far-fields were recovered, but now also involved C_μ, $C_{\epsilon 2}$ and $C_{\epsilon 1}$. This allowed us to compute the trajectory and circulation of the CVP as a function of the analytical estimate of $\mathbf{C} = (C_\mu, C_{\epsilon 2}, C_{\epsilon 1}) = \mathbf{C}_a$ and compare with compressible experiments described in Ref. [3, 5]. This was done in our conference paper [13] where we found good agreement with $M = 0.6, 0.7$ and $0.8, J = 10.2$ experiments. Our model was derived under an incompressibility assumption, implying that the effect of compressibility on the JIC interaction in the experiments we will calibrate to is weak.

B. Improving $k-\epsilon$ models

$k-\epsilon$ RANS models contain grossly simplified representations of turbulent processes, along with numerical parameters. The numerical parameters are estimated from turbulent boundary layers and free shear flows [18]; we will refer to them as the "nominal" values $\mathbf{C}_{nom}$. They are not universal, and RANS model parameters have been repeatedly tuned for particular classes of flows [19]. $k-\epsilon$ models have also been augmented with extra terms, e.g., for axisymmetric and compressible jets [20, 21]. The fitting of $k-\epsilon$ models to measurements of velocity profiles of supersonic axisymmetric jets revealed model parameters that are quite different from $\mathbf{C}_{nom}$. In particular, their estimate of $C_{\epsilon 2}$ is close to its upper bound of 2.1.

Recently, the estimation of RANS parameters have tended to adopt a Bayesian approach, computing the parameters' JPDF from experimental and DNS (Direct Numerical Simulation) data. This decision is partly driven by the realization that the data may not be uniformly informative on the RANS constants being estimated, or they may be affected by the inherent shortcomings of RANS models. The first investigations targeted simple flows e.g., flat-plate boundary layers and wall-bounded flows [22, 23]. Bayesian model averaging has also been used to "merge" JPDFs of RANS constants obtained from a variety of flow cases (favorable and adverse pressure gradients) and a host of $k-\omega$, $k-\epsilon$ and Spalart-Allmaras models [24]. Bayesian calibration of RANS constants have also been explored in more complicated (3D) geometries. In Ref. [25], the authors calibrated a $k-\epsilon$ model for urban canyon flows, whereas in Refs. [9, 11], we addressed compressible jet-in-crossflow interactions. The method developed in Ref. [9] is the one employed for Bayesian calibration results presented in this paper. These more complicated and computationally expensive RANS simulations had to employ statistical emulators with Markov chain Monte Carlo (MCMC) sampling to construct the JPDF and also take recourse to informative priors, since RANS constants arbitrarily picked from within their bounds will not necessarily provide realistic flowfields (or even allow the simulation to complete). Bayesian estimation of parameters of $k-\omega-\gamma$ models, for transitional hypersonic flat-plate boundary layers, have successfully used generalized polynomial chaos expansions to construct statistical emulators and infer six parameters from experimental

measurements of Stanton number [26]. The approach is very similar to the method used in this paper, though we do not use polynomial chaos expansion emulators. Bayesian estimation of $k-\omega$ RANS constants have also been performed using iterated Ensemble Transform Kalman Filters using measurements from an experiment of a flow over a backward facing step [27]. The use of an "online" method such as Kalman filters, which assimilate data incrementally for Bayesian estimation of turbulence model parameters, can be helpful when calibration datasets are too large for "batch" methods such as MCMC. DNS simulations provide such datasets.

Most RANS models employ a linear eddy viscosity model (LEVM) which cannot reproduce the anisotropy observed in turbulent flows. Much work on data-driven estimation of corrections/augmentation of RANS models aim to rectify this shortcoming. In Ref. [28], the authors estimated spatially variable corrections, modeled as a Gaussian random field, to the eddy viscosity coefficient using DNS data. In addition, Ref. [29] developed a genetic algorithm to discover stress-strain rate relationships using DNS datasets of flow over backward facing step and tested them by predicting flows over periodic hills. In Ref. [30], the authors developed a parametric model for the anisotropy in turbulent stresses; the parameters are functions of space. These have been modeled as Gaussian random fields and inferred from DNS data [31]. These corrections for anisotropy were related to local flow properties using random forests [32]. In other work, spatially variable corrections to the eddy viscosity evolution equation (Spalart-Allmaras RANS model) were estimated using full-field (Bayesian) inversion employing DNS [33] and experimental [34] data of flows over airfoils. They were related to local flow properties using artificial neural networks. Recently, Edeling et al developed transport equations for anisotropy perturbation to turbulent stresses and reduced the field inversion to that of estimating 2 parameters; they demonstrated their method by predicting flow over a backward facing step and a subsonic jet flow [35]. Thus there exist methods to enrich RANS equations to reduce model-form errors, although they may require the solution of a challenging inverse problem.

Ling et al. [36] estimated turbulent stress anisotropy by comparing DNS and RANS simulations and modeled the anisotropy using a neural network that specifically constrained the modeled tensor to be Galilean invariant. The neural net model was integrated into a $k-\epsilon$ RANS simulator and used to predict phenomena that cannot be captured by LEVMs. Ling's approach does not require one to solve an inverse problem. It has been used to model turbulent wall fluctuations [37] and learning turbulent diffusivity for film cooling flows [38]. Such methods could be used to improve RANS once shortcomings due to the use of inappropriate parameters have been be rectified.

III. Inverse modeling

A. The flow problem

The wind-tunnel experiments and measurements that have been used in this paper are fully described in Refs. [3, 5]. The computational details of the CFD simulator used in this paper are in our previous paper [9]; consequently, we only

provide a summary here. A schematic diagram of the wind-tunnel test section is in Fig. 1 (left). A jet of diameter 9.53 mm is introduced, at Mach 3.93, into a crossflow from an orifice located at the front (left side) of the test section floor. Separate experiments are conducted by varying the crossflow Mach number $M = \{0.6, 0.7, 0.8\}$. The ratio of the jet momentum to that of the crossflow, J, is held fixed at 10.2 in these experiments. Experiments are also performed by varying $J = \{10.2, 16.7\}$, with the crossflow Mach number M fixed at 0.8. PIV measurements of the mean flow velocity are made on two planes - the mid-plane (the plane of symmetry in Fig. 1 (left)), and the cross-plane, the transverse plane that slices through the CVP as seen in Fig. 1 (right). We also plot a window $\mathcal{W}$ where quantifications of vorticity will be done in Sec. V. The cross-plane is situated 321.8 mm downstream of the jet, and the oppositely-signed vortices are clearly seen in the figure.

Mid-plane mean-flow velocity measurements are made at 5 streamwise locations, the first being 200 mm downstream of the jet, and the rest at 50 mm intervals proceeding downstream. At each of these five locations, velocity measurements are available at 63 points, distributed vertically, which we refer to as "probes". Mid-plane measurements are available for all the experiments. Cross-plane measurements are available only for the $M = 0.8$ experiments. Since they are available for all the experiments, we will use mid-plane measurements of streamwise and vertical velocities in our inverse problem to infer $\mathbf{C}$. We will check the predictive skill of the calibrated $\mathbf{C}$ using measurements on the cross-plane. Note that this necessarily means that we can perform the check only for the subset of the experiments where both types of measurements are available. Note, too, that this is different from our previous work [9] where calibration was performed using cross-plane measurements obtained solely from the $(M = 0.8, J = 10.2)$ experiment.

The calibration of $\mathbf{C}$ employs a $k-\epsilon$ RANS model, with a compressibility correction; details are in Refs. [9, 39]. As verified in Ref. [9], the most important $k-\epsilon$ constants for the JIC interaction are $\mathbf{C} = (C_\mu, C_{\epsilon 2}, C_{\epsilon 1})$. They will be the targets of our calibration study. Our flow simulator, SIGMA CFD (Sandia Implicit Generalized Multi-Block Analysis Code for Fluid Dynamics), employs Roe-TVD fluxes with a minmod limiter to approximate the spatial terms in the $k-\epsilon$ RANS equation. Integration in time is performed using a first-order point-implicit scheme. The computations start with first-order spatial discretization, proceed for 5,000 timesteps, and are then switched to a second-order method for another 25,000 timesteps. Convergence to a steady state is carried out using local time-stepping, as the CFL is gradually ramped up. We use a multi-block mesh with about 10 million cells; mesh convergence studies are in Ref. [8]. Initial and boundary conditions are described in detail in one of our previous papers [9].

B. Formulation of the Bayesian inverse problem

In this section, we formulate a Bayesian inverse problem to infer a JPDF for $\mathbf{C} = (C_\mu, C_{\epsilon 2}, C_{\epsilon 1})$ conditional on streamwise and vertical mean flow velocities measured on the mid-plane. Since it is the plane of symmetry, there is no spanwise velocity. Henceforth any references to a calibrated set of $k-\epsilon$ constants $\mathbf{C}$ will imply the JPDF, rather than a deterministic or point estimate of $\mathbf{C}$. Computing $\mathbf{C}$ as a JPDF captures the uncertainty in the estimate due to

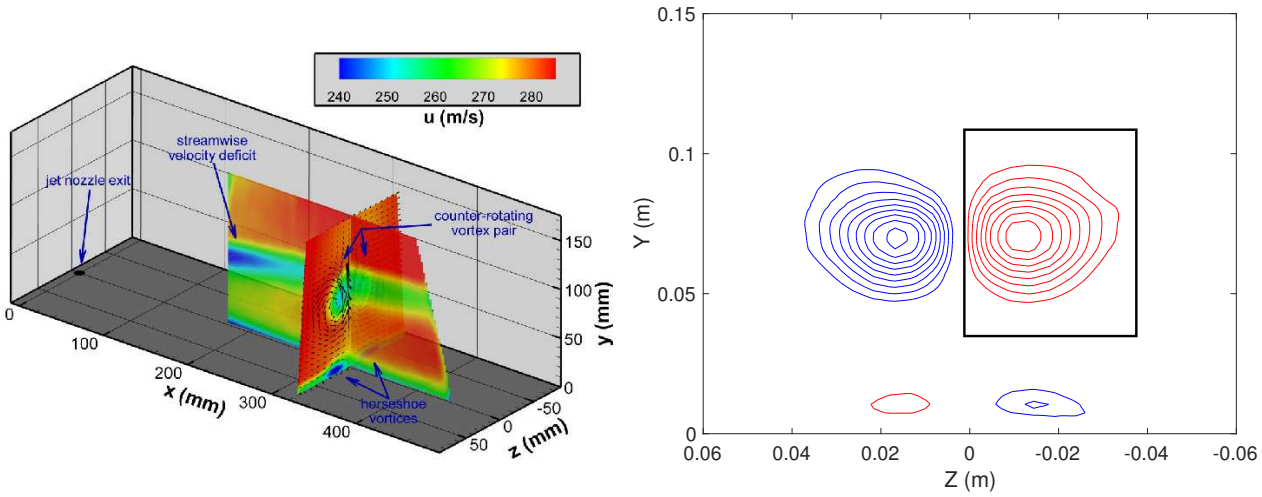

Fig. 1 Left: Schematic of the wind-tunnel test section, which also serves as the computational domain. The orifice where the jet is introduces is also shown, as are the mid-plane and the cross-plane. Right: Contour plot of the vorticity field on the cross-plane slicing through the CVP. Positive vorticity is plotted with red contours. We also plot a window $\mathcal{W}$ where quantifications of vorticity will be performed in Sec. V.

limited measurements, measurement noise and the shortcomings of the RANS model that prevent it from reproducing experimental measurements perfectly. The development closely parallels the formulation of the Bayesian inverse problem in Ref. [9], which used measurements on the cross-plane. Cross-plane measurements are available for only a subset of the experiments described in Refs. [3, 5], necessitating the development of this alternative inverse problem formulation.

Consider an experimental dataset consisting of a vector $\mathbf{y}_e$, of length N_p, containing measurements at N_p probes. Assume that a simulation seeded with the $k-\epsilon$ constants $\mathbf{C}$ results in numerical predictions $\mathbf{y}_m(\mathbf{C})$ at the same probe locations. We relate the measurements to the model predictions thus: $\mathbf{y}_e = \mathbf{y}_m(\mathbf{C}) + \boldsymbol{\epsilon}$, where $\boldsymbol{\epsilon} = \{\epsilon_i\}, i = 1 \ldots N_p$ is the model - data mismatch. It is a composite of measurement and model-form errors. We define model-form errors as the discrepancy between noise-free observations and model predictions using a value of $\mathbf{C}$ that is optimal across all JIC interactions. We make the inverse modeling assumption that the error at each probe is independent of the others, and can be modeled as independently and identically distributed Gaussians i.e., $\epsilon_i \sim \mathcal{N}(0, \sigma^2)$. This statistical representation for the model - data mismatch introduces an extra parameter σ, which will also be estimated as a part of the calibration; its provides a crude measure of disagreement between model predictions and experimental observations. If the measurement errors in the experiment are small, σ is a measure of the model-form error in $k-\epsilon$ RANS when simulating the JIC experiment.

We now develop the expression for the JPDF of $(\mathbf{C}, \sigma^2)$ conditional on the experimental data $\mathbf{y}_e$ i.e., $P(\mathbf{C}, \sigma^2|\mathbf{y}_e)$. Given our Gaussian model for the model-data mismatch $\epsilon_i \sim \mathcal{N}(0, \sigma^2)$, the likelihood $\mathcal{L}(\mathbf{y}_e|\mathbf{C})$ of observing $\mathbf{y}_e$ when

the CFD simulator is seeded with $\mathbf{C}$ is

$$\mathcal{L}(\mathbf{y}_e|\mathbf{C},\sigma^2) \propto \frac{1}{\sigma^{N_p}} \exp\left(-\frac{||\mathbf{y}_e - \mathbf{y}_m(\mathbf{C})||_2^2}{2\sigma^2}\right). \tag{1}$$

Assume that our prior belief regarding $\mathbf{C}$ and σ^2 can be expressed as the distributions $\Pi_1(\mathbf{C})$ and $\Pi_2(\sigma^2)$. By Bayes' theorem, these can be combined into an expression for $P(\mathbf{C},\sigma^2|\mathbf{y}_e)$, the posterior density (alternatively, the JPDF):

$$P(\mathbf{C},\sigma^2|\mathbf{y}_e) \propto \mathcal{L}(\mathbf{y}_e|\mathbf{C},\sigma^2)\ \Pi_1(\mathbf{C})\ \Pi_2(\sigma^2) \propto \frac{1}{\sigma^{N_p}} \exp\left(-\frac{||\mathbf{y}_e - \mathbf{y}_m(\mathbf{C})||_2^2}{2\sigma^2}\right) \Pi_1(\mathbf{C})\ \Pi_2(\sigma^2). \tag{2}$$

The actual calibration variables are the *velocity deficit in the streamwise direction* u_{def} and the *normalized vertical velocity* on the mid-plane v_{norm}. We formally define them as

$$u_{def} = \frac{U_{max}(x) - u}{U_\infty} \quad \text{and} \quad v_{norm} = \frac{v}{U_\infty},$$

where $U_{max}(x)$ is the maximum streamwise velocity at an x-location and U_∞ is the freestream velocity. Due to the mass added by the jet, the maximum velocity observed in the test section varies in the streamwise direction. u_{def} and v_{norm} are the elements of $\mathbf{y}_e$. Define $\mathbf{u}_m$ to be the predicted streamwise velocity deficit u_{def} and $\mathbf{v}_m$ be the normalized vertical velocity v_{norm} for all the probes. Define $\mathbf{u}_e$ and $\mathbf{v}_e$ to be their experimental counterparts over all the probes. Therefore, Eq. 2 can be written as

$$P(\mathbf{C},\sigma^2|\mathbf{u}_e,\mathbf{v}_e) \propto \frac{1}{\sigma^{N_p}} \exp\left(-\frac{||(\mathbf{u}_e - \mathbf{u}_m(\mathbf{C}))/K_u||_2^2}{2\sigma^2}\right) \exp\left(-\frac{||(\mathbf{v}_e - \mathbf{v}_m(\mathbf{C}))/K_v||_2^2}{2\sigma^2}\right) \Pi_1(\mathbf{C})\ \Pi_2(\sigma^2), \tag{3}$$

where $K_u = \max(\mathbf{u}_e)$ and $K_v = \max(\mathbf{v}_e)$. Normalization using K_u and K_v ensures that the contributions from u_{def} and v_{norm} are equally weighted in the expression for the posterior density. Solving Eq. 3 requires us to specify $\Pi_1(\mathbf{C})$ and $\Pi_2(\sigma^2)$. As in Ref. [9], we represent our prior belief of σ^2 in terms of its reciprocal i.e., $\Pi_2(\sigma^{-2})$ which we model with a Gamma distribution i.e., $\sigma^{-2} \sim \Gamma(k,\theta)$, where $k = 1, \theta = 1$. Such a prior distribution is called an inverse Gamma prior and has the advantage of being practically non-informative for $\sigma^{-2} > 5$. This ensures that our prior beliefs do not influence the inference of σ^2 excessively, and the JPDF should reflect the information on σ^2 contained in the experimental measurements.

The four-dimensional distribution $P(\mathbf{C},\sigma^2|\mathbf{u}_e,\mathbf{v}_e)$ in Eq. 3 is complicated, and is realized by drawing samples of $(\mathbf{C},\sigma^2)$. As in Ref. [9], the sampling is performed using a particular MCMC algorithm called Delayed Rejection Adaptive Metropolis [40]. The conjugate inverse Gamma prior for σ^2 allows us to sample for σ^{-2} via a Gibbs sampler. The MCMC chain is run till it converges to a stationary distribution, as assessed using the Raftery-Lewis method [41]. The software for computing $P(\mathbf{C},\sigma^2|\mathbf{u}_e,\mathbf{v}_e)$ is written in R [42]. We use the Delayed Rejection Adaptive Metropolis

algorithm implemented in the R package FME [43]. We also use the R package mcgibbsit [44] for its implementation of the Raftery-Lewis convergence metric. The samples of $(\mathbf{C}, \sigma^2)$ are used to construct the JPDF $P(\mathbf{C}, \sigma^2|\mathbf{u}_e, \mathbf{v}_e)$ empirically via kernel density estimation [45].

The MCMC method takes between 25,000 – 50,000 samples of $(\mathbf{C}, \sigma^2)$ to reach convergence. Since each sample requires one to run a 3D JIC RANS simulation to produce $(\mathbf{u}_m(\mathbf{C}), \mathbf{v}_m(\mathbf{C}))$, the MCMC method is impractical as described above. Instead, we replace the RANS simulator with a statistical emulator. The emulator is a computationally inexpensive proxy of SIGMA CFD that can provide accurate approximations of $(\mathbf{u}_m(\mathbf{C}), \mathbf{v}_m(\mathbf{C}))$ within the parameter space C defined by:

$$\begin{aligned} 0.06 &\leq C_\mu \leq 0.12, \\ 1.7 &\leq C_{\epsilon 2} \leq 2.1, \\ 1.2 &\leq C_{\epsilon 1} \leq 1.7. \end{aligned} \tag{4}$$

C. Priors and statistical emulators

An informative prior $\Pi_1(\mathbf{C})$: The bounds on $C_\mu, C_{\epsilon 2}$ and $C_{\epsilon 1}$ defined in Eq. 4 could be used to propose a prior distribution $\Pi_1(\mathbf{C})$, e.g., as a uniform distribution on C. However, an arbitrary point in C may not lead to a physically realistic combination $(C_\mu, C_{\epsilon 2}, C_{\epsilon 1})$ - the RANS simulation may not run, fail to converge to a steady state or predict a flow field that does not resemble transonic, high Reynolds number flows. Thus, in order to construct $\Pi_1(\mathbf{C})$, we will first need to isolate a physically realistic region $\mathcal{R} \subset C$ in the parameter space. In doing so, we will follow the method developed in our previous paper on RANS calibration [9], and so we summarize the process here.

The prior $\Pi_1(\mathbf{C})$ is constructed during the process of devising a statistical emulator for SIGMA CFD. We distribute 2744 $(= 14^3)$ samples of $\mathbf{C}$ inside C using a quasi-random, space-filling Halton sequence and seed RANS JIC simulations with them. Of these a few simply fail to converge to a steady state (due to non-physical $(C_\mu, C_{\epsilon 2}, C_{\epsilon 1})$ combinations) while others run to completion but may provide unsteady or unrealistic flowfields. We compute the RMS (root mean square) discrepancy between $(\mathbf{u}_e, \mathbf{v}_e)$ and $(\mathbf{u}_m, \mathbf{v}_m)$ produced by each of the RANS simulations, and retain the top 25% of the run i.e., the ones closest to the experimental measurements. The values of $\mathbf{C}$ so chosen are deemed to constitute $\mathcal{R}$, the physically realistic subset of the parameter space C. As in Ref. [9], we define

$$\Pi_1(\mathbf{C}) = \begin{cases} 1 & \text{if } \mathbf{C} \in \mathcal{R} \\ 0 & \text{otherwise} \end{cases} \tag{5}$$

For the particular case of the $(M = 0.8, J = 10.2)$ experiment, of the 2744 runs, 2628 completed. Of these the top 25% i.e., 657 were used to define $\mathcal{R}$; they are plotted in Fig. 2. We note that they constitute a contiguous region in C.

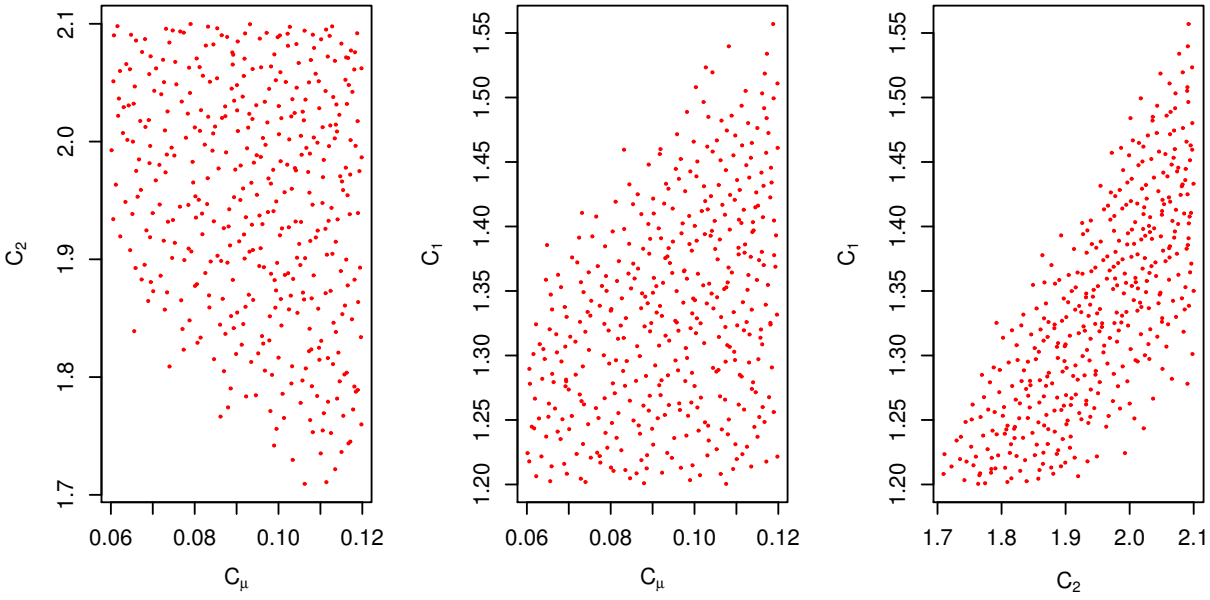

Fig. 2 C points in C that constitute $\mathcal{R}$, projected down to the $(C_\mu, C_{\epsilon 2})$, $(C_\mu, C_{\epsilon 1})$ and $(C_{\epsilon 2}, C_{\epsilon 1})$ planes.

The discrete values of $\Pi_1(\mathbf{C})$, as initialized using Eq. 5, constitute the training data (TD) to construct a binary support vector machine classifier (SVMC). For the particular case of the ($M = 0.8, J = 10.2$) experiment, the TD consisted of 2628 records, of which 657 fell in one class. The process for constructing the SVMC, and the R package used to do so, are described in Ref. [9]. We ensure that the SVMC has a misclassification rate of less than 10% and thus can define $\mathcal{R}$ accurately inside C. We use this SVMC as an implementation of the prior $\Pi_1(\mathbf{C})$ in Eq. 3, integrate it into the MCMC software, and use it to sample posterior density $P(\mathbf{C}, \sigma^2 | \mathbf{u}_e, \mathbf{v}_e)$.

Statistical emulator for SIGMA CFD: We use polynomial curve-fits to map the inputs into SIGMA CFD i.e., $(C_\mu, C_{\epsilon 2}, C_{\epsilon 1})$, to the outputs u_{def} and v_{norm}. These curve-fits are then used as computationally inexpensive proxies for our RANS simulator. Separate curve-fits are constructed for u_{def} and v_{norm}, and probes are also treated individually. At each probe, we postulate a cubic polynomial in $(C_\mu, C_{\epsilon 2}, C_{\epsilon 1})$ as a model for u_{def} (or v_{norm}). We use the values of $\mathbf{C}$ that lie in $\mathcal{R}$ as the data in a least-squares fit to estimate the polynomial's coefficients. The polynomial is simplified using Akaike Information Criterion. We find that many of the cubic terms are removed, and in case of some probes, the polynomial model reduces to a quadratic. Before using the polynomial model as a replacement for SIGMA CFD in the inverse problem, we ensure that it is an accurate proxy. We compute the approximate error of the polynomial emulator using repeated random subsampling, a form of cross-validation; only those emulators that achieve an approximation error less than 15% are retained. We see that this process often removes about 2/3rd of polynomial proxies, and the probes with accurate emulators follow the trajectory of the jet. This is not unexpected - the impact of varying $\mathbf{C}$ is felt in

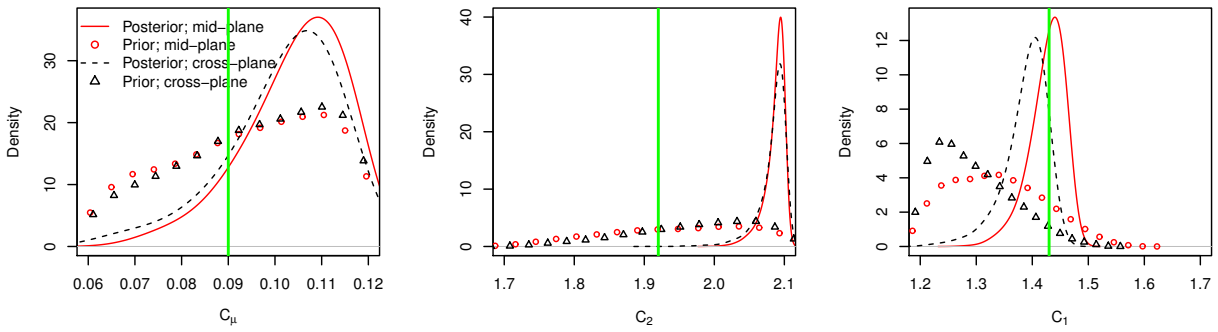

Fig. 3 Prior and posterior densities obtained from mid-plane and cross-plane measurements. Posterior densities obtained from mid-plane and cross-plane measurements are plotted using solid and dashed lines respectively. The corresponding priors are plotted with ∘ and △. The vertical lines are the "nominal" values of the parameters.

regions with substantial velocity gradients and turbulence. The run-to-run variation in the regions of the flowfield away from the jet is small and mostly due to numerical noise, which cannot be modeled with $(C_\mu, C_{\epsilon 2}, C_{\epsilon 1})$. An illustration of such "model-able" probes tracking the jet trajectory can be found in Ref. [12], Fig.2. Note that as in Ref. [9], no emulators are built for probes inside the boundary layer; the calibration is aimed at the accurate simulation of the jet, the CVP and their trajectory.

The procedure outlined in Sec. III.B and III.C is repeated for all 4 experiments considered in this study, resulting in 4 JPDFs $P(\mathbf{C}, \sigma^2 | \mathbf{u}_e, \mathbf{v}_e)$. However, to be useful, we have to ensure that the information content in $(\mathbf{u}_e, \mathbf{v}_e)$ on $(C_\mu, C_{\epsilon 2}, C_{\epsilon 1})$ is substantial, preferably similar to that of the cross-plane measurements, as assessed in Ref. [9]. We check this in two ways. First, we compare the JPDF $P(\mathbf{C}, \sigma^2 | \mathbf{u}_e, \mathbf{v}_e)$ for the $(M = 0.8, J = 10.2)$ experiment with the one inferred from cross-plane measurements in Ref. [9]. This is shown in Fig. 3. There, the posterior density obtained using mid-plane measurements is plotted using a solid line, while the one from Ref. [9], inferred using cross-plane measurements, is plotted using a dashed line. Prior densities, which are the projections of $\mathcal{R}$ onto the axes, are plotted with ∘ and △ for the mid-plane and cross-plane cases respectively. We see that the prior densities are very close, indicating that the physically realistic parameter space $\mathcal{R}$ identified in this paper using u_{def} and v_{norm} may be very similar to the one identified in Ref. [9] using cross-plane measurements. Also the prior distribution is sufficiently wide to comfortably contain the posterior density. We take this as a sign that the procedure for identifying and enforcing $\mathcal{R}$, using the 25% threshold described above, is not restrictive. Further, the posterior densities are almost identical, indicating that the information on $(C_\mu, C_{\epsilon 2}, C_{\epsilon 1})$ contained in the mid-plane measurements may be similar to the information contained in the cross-plane measurements. The vertical lines in the figures denote the "nominal" values of C_μ, $C_{\epsilon 2}$ and $C_{\epsilon 1}$, and are quite different from the *maximum a posterior* (MAP) values (the peak of the PDF).

The close agreement between the two posterior densities in Fig. 3 implies that they are equally predictive. This

can be checked using a "pushed-forward posterior" test and is documented in Ref. [12]. We seed our RANS simulator (SIGMA CFD) with 100 samples of $\mathbf{C}$ drawn from $P(\mathbf{C}, \sigma^2|\mathbf{u}_e, \mathbf{v}_e)$ and develop an ensemble of velocity predictions on the cross- and mid-planes. These are compared to flowfields developed using a similar "pushed-forward posterior" test with samples drawn from the JPDF inferred using cross-plane measurements. The comparison is available in Figs. 5 and 6 in our conference paper [12] and the two ensembles match very closely. This is not surprising, given the agreement between the two JPDFs. This gives us some confidence that the mid-plane and cross-plane measurements contain similar levels of information on $(C_\mu, C_{\epsilon 2}, C_{\epsilon 1})$. This is important since two of the four experiments considered in this paper *viz*, the $(M = 0.6, J = 10.2)$ and $(M = 0.7, J = 10.2)$ experiments, do not have cross-plane measurements and we have no independent way of checking whether the experiments' JPDF can reproduce flowfield measurements that were *not* used in the calibration.

The bulk of the computational cost is incurred in generating the TD. Each SIGMA CFD simulation of a JIC interaction requires about 12 hours on 1024 cores of a PowerPC A2 processor; 2744 runs are required to generate the TD for a given experiment. We generate TDs for four separate experiments corresponding to $(M = 0.6, J = 10.2)$, $(M = 0.7, J = 10.2)$, $(M = 0.8, J = 10.2)$ and $(M = 0.8, J = 16.7)$. The "pushed-forward posterior" tests require additional runs. Simulations were performed on the Sequioa supercomputer (`https://asc.llnl.gov/computing_resources/sequoia/`) at Lawrence Livermore National Laboratory.

IV. Analytical model

Hasselbrink and Mungal [14] described, in a JIC interaction, the existence of a near-field, where the trajectory of the jet scaled as $y \sim x^{1/2}$, and a far-field where the scaling proceeded as $y \sim x^{/13}$. We will use their formalism to develop our analytical model, starting from the $k - \epsilon$ RANS equations, so that we may obtain analytical estimates for $C_\mu, C_{\epsilon 2}$ and $C_{\epsilon 1}$. We first check whether $k - \epsilon$ RANS equations show these scaling for compressible JIC interactions. In Fig. 4 we plot the scaled trajectories for a $J = 10.2$ jet interacting with a $M = 0.6$ crossflow, simulated using the nominal values of the RANS constants $\mathbf{C}_{nom}$. The simulation domain and settings are the same as the one described in Sec. III.A. The location of the jet, at any x (streamwise) location is the y (vertical) location where the vertical normalized velocity v_{norm} reaches a maximum. We represent $y = Cx^n$ as the trajectory and fit this model to the RANS data. In Fig. 4, we plot $C = y/x^{1/3}$ using $\circ$ and $C = y/x^{1/2}$ using $\times$. We clearly see the two scalings fitting the trajectory. For $x/d_j > 13$ (the vertical line), C assumes a constant value of around 2.9; further, for $x/d_j < 13$, C varies between 2 and 2.9. On the other hand, when we plot $C = y/x^{1/2}$, C assumes a value of around 1.8 for $x/d_j < 13$, and then slowly decays. Thus the separation of near-field and far-field behaviors, described in Ref. [14], are replicated here. This gives us confidence that an analytical model that draws from a $k - \epsilon$ model could accurately represent the data in Ref. [3, 5].

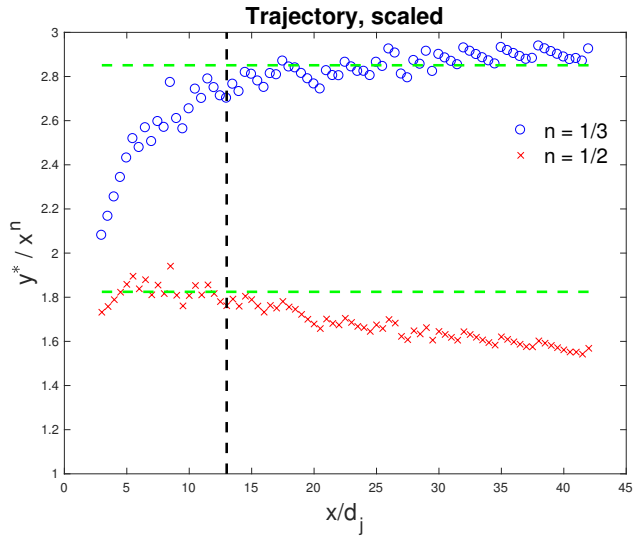

Fig. 4 Trajectory of a $(M = 0.6, J = 10.2)$ **JIC interaction, simulated using** $k - \epsilon$ **RANS equations, scaled as** $y = Cx^n$**. We plot** $C = y/x^{1/3}$ **using** $\circ$ **and** $C = y/x^{1/2}$ **using** $\times$**. There are two significantly different regimes for the trajectory, separated by the vertical line at** $x/d_j = 13$**.**

A. Far-field model

We develop a self-similar model for the far-field first. It follows the development of a similar model for wakes [10], in keeping with its similarity with the far-field behavior of JIC [14]. We assume that the far-field interactions are only weakly compressible, and we will develop the model under incompressibility and axisymmetric assumptions where the $x - r$ plane contains the jet. We also assume that the jet, which was introduced vertically, has curved into the crossflow to an extent that the vertical velocity in the jet is small i.e. $v/U_\infty << 1$. We also assume that the mass flow and momentum of the jet (in magnitude) is the same as when it was introduced into the crossflow. The center of the jet has a streamwise velocity deficit that changes downstream, and we will model the velocity deficit profile at a given x location, in a manner similar to wakes. The details of the derivation are in Ref. [13].

Let $u = U_\infty + \hat{u}, \hat{u}/U_\infty \ll 1$. We also set

$$\hat{u} = \widehat{u_s}(x) f(\xi), k = k_s(x) g(\xi) \text{ and } \epsilon = \epsilon_s(x) h(\xi), \tag{6}$$

where $l = l(x)$ is a turbulence length scale and $\xi = r/l$. Under the assumption of incompressibility and negligible vertical velocity, the momentum equation can be linearized as

$$U_\infty \frac{\partial u}{\partial x} = \frac{1}{r}\frac{\partial}{\partial r}\left(rC_\mu \frac{k^2}{\epsilon}\frac{\partial u}{\partial r}\right), \tag{7}$$

where we have used a linear eddy viscosity model for the turbulent kinematic viscosity $\nu_T = C_\mu k^2/\epsilon$. We write

$$\frac{\partial u}{\partial x} = \frac{\partial \hat{u}}{\partial x} = \widehat{u_s}' f - \widehat{u_s}\xi f' \frac{l'}{l}$$

and substitute into Eq. 7 to get

$$U_\infty \left(\widehat{u_s}' f - \widehat{u_s}\xi f' \frac{l'}{l} \right) = C_\mu \frac{k_s^2 \widehat{u_s}}{\epsilon_s l^2} \frac{1}{\xi} \frac{\partial}{\partial \xi} \left(\xi f' \frac{g^2}{h} \right) \tag{8}$$

Here prime ($'$) denotes a first derivative with respect to the independent variable which is x in case of l' and ξ in case of f'. We define $k_s = C\widehat{u_s}^2$ and $\epsilon_s = D\widehat{u_s}^3/l$, which we substitute into Eq. 8, and divide both sides by $\widehat{u_s}^2/l$, to get

$$\frac{\widehat{u_s}' f - \widehat{u_s}\xi f' l'/l}{\widehat{u_s}^2/l} = \frac{C_\mu}{U_\infty} \frac{1}{\xi} \frac{\partial}{\partial \xi} \left(\xi f' \frac{g^2}{h} \right) \frac{C^2}{D}.$$

The right hand side of the equation is solely a function of ξ, which implies

$$\frac{l}{\widehat{u_s}^2} \frac{\partial \widehat{u_s}}{\partial x} = K_1 \quad \text{and} \quad \frac{1}{\widehat{u_s}} \frac{\partial l}{\partial x} = K_2. \tag{9}$$

Eq. 9 holds if

$$\widehat{u_s} = A x^{n-1} \quad \text{and} \quad l = B x^n. \tag{10}$$

The streamwise momentum flux integrated across the jet at any x location is

$$2\pi\, \dot{m} \int_0^\infty u\, r\, dr = 2\pi\, \dot{m}\, l^2 \int_0^\infty (U_\infty + \hat{u}) \xi d\xi, \tag{11}$$

where $\dot{m} = \rho_\infty U_\infty$ is the mass flux and ρ_∞ is the freestream crossflow density. This momentum consists of the momentum due to the crossflow $\dot{m} U_\infty$ and that due to the jet. Equating the jet's contribution to the momentum to the jet's momentum at the jet exit at the bottom of the test section, we get

$$\frac{\pi}{4} d_j^2 \rho_j V_j^2 = 2\pi l^2 \widehat{u_s} \rho_\infty U_\infty \int_0^\infty \xi f d\xi \tag{12}$$

Since the left hand side is a constant, $l^2 \widehat{u_s}$ too should be a constant. From Eq. 10 we get

$$3n - 1 = 0 \quad \text{or} \quad n = 1/3 \tag{13}$$

Combining Eq. 13 and Eq. 9, we get

$$\widehat{u_s} = A^* U_\infty d_j^{2/3} x^{-2/3} \quad \text{and} \quad l = B^* d_j^{2/3} x^{1/3}, \tag{14}$$

where A^* and B^* are non-dimensional. We substitute Eq. 14 into Eq. 8 to get

$$-\frac{B^*}{3A^*}\frac{D}{C^2 C_\mu}\left(2f + \xi f'\right) = \frac{1}{\xi}\frac{\partial}{\partial \xi}\left(\xi f' \frac{g^2}{h}\right). \tag{15}$$

Following the modeling of wakes [46], we set

$$\frac{D}{C^2 C_\mu} = \mathrm{Re_T} = 14.1 \quad \text{and} \quad \frac{g^2}{h} = 1, \tag{16}$$

where Re_T is the turbulence Reynolds number and is set to 14.1 per Ref. [47]. In Eq. 16, set

$$-\frac{B^*}{3A^*}\frac{D}{C^2 C_\mu} = \alpha = 1, \ \text{ to get } \ -\frac{B^*}{3A^*} = \mathrm{Re_T}^{-1}. \tag{17}$$

From Eq. 15 we get

$$2f + \xi f' = \frac{1}{\xi}\frac{\partial}{\partial \xi}\left(\xi f'\right), \ \text{ implying } \ f = \exp\left(-\frac{\xi^2}{2}\right). \tag{18}$$

Using Eq. 12, we also get

$$\frac{J}{8} = A^* (B^*)^2, \tag{19}$$

where J is the jet-to-crossflow momentum ratio. Using Eq. 19 and Eq. 17 to compute A^* and B^* and substituting into Eq. 14, we get

$$\begin{aligned} \frac{\widehat{u_s}}{U_\infty} &= \frac{1}{2}\left(\frac{\mathrm{Re_T}}{3}\right)^{2/3} J^{1/3}\left(\frac{d}{x}\right)^{2/3} \\ \frac{l}{d_j} &= \frac{1}{2}\left(\frac{3}{\mathrm{Re_T}}\right)^{1/3} J^{1/3}\left(\frac{x}{d}\right)^{1/3}. \end{aligned} \tag{20}$$

B. $k-\epsilon$ parameter estimates

We use the far-field profiles developed in Sec. IV.A to derive expressions for $C_{\epsilon 2}, C_\mu$ and $C_{\epsilon 1}$. We linearize the evolution equations for k and ϵ as we had done for Eq. 7 to get

$$U_\infty \frac{\partial k}{\partial x} = \frac{1}{r}\frac{\partial}{\partial r}\left(r \frac{C_\mu}{\sigma_k}\frac{k^2}{\epsilon}\frac{\partial k}{\partial r}\right) + C_\mu \frac{k^2}{\epsilon}\left(\frac{\partial u}{\partial r}\right)^2 - \epsilon$$

for the $k-$equation and, for the $\epsilon-$equation:

$$U_\infty \frac{\partial \epsilon}{\partial x} = \frac{1}{r}\left(r\frac{C_\mu}{\sigma_\epsilon}\frac{k^2}{\epsilon}\frac{\partial}{\partial r}\epsilon\right) + C_{\epsilon 1}C_\mu k\left(\frac{\partial}{\partial r}u\right)^2 - C_{\epsilon 2}\frac{\epsilon^2}{h}.$$

Introducing the expressions in Eq. 6, with $k_s = C\widehat{u_s}^2$ and $\epsilon_s = D\widehat{u_s}^3/l$, with $\widehat{u_s}$ and l replaced by the expressions in Eq. 20, we get,

$$\begin{aligned} \alpha\,(2g + \xi g') \quad &+ \quad \frac{1}{\xi}\frac{\partial \xi g'}{\partial \xi} + \frac{1}{C}\,(f')^2 - \mathrm{Re_T}\frac{D}{C}h = 0 \\ \alpha\,(4h + \xi h') \quad &+ \quad \frac{1}{\xi}\frac{\partial}{\partial \xi}\xi h' + \frac{C_{\epsilon 1}}{C}\,(f')^2 - C_{\epsilon 2}\mathrm{Re_T}\frac{D}{C}\frac{h^2}{g} = 0. \end{aligned} \tag{21}$$

Recall that in Eq. 16, we had stated that $g^2/h = 1$. We approximate this as $h = g^2 \approx \bar{g}g$, where $\bar{g}$ is the mean value of g over the $k-$profile. We substitute in Eq. 21 (the $k-$equation) and also set $\alpha = 1$, to get

$$2g + \xi g' + \frac{1}{\xi}\frac{\partial}{\partial \xi}\xi g' + \frac{1}{C}\,(f')^2 - \mathrm{Re_T}\frac{D}{C}\bar{g}g = 0.$$

If we demand that

$$\bar{g}\mathrm{Re_T}\frac{D}{C} = 2, \tag{22}$$

then the equation for k simplifies to

$$\xi g' + \frac{1}{\xi}\frac{\partial}{\partial \xi}\xi g' + \frac{1}{C}\,(f')^2 = 0, \tag{23}$$

leading to a solution for g

$$g = \frac{1}{2C}\left(2\,\mathrm{Ei}\left(\frac{\xi^2}{2}\right) - 2\,\mathrm{Ei}(\xi^2) - \exp(-\xi^2)\right), \tag{24}$$

where

$$\mathrm{Ei}(x) = \int_x^\infty \frac{\exp(-u)}{u}du$$

are exponential integrals. This allows $g'(\xi = 0) = 0$ and $g(\infty) = 0$ which satisfy the boundary conditions for the $k-$profile. Also we approximate $\bar{g}$ as

$$\bar{g} = \frac{1}{2}\,(g(0) + g(\infty)) = \frac{1}{4C}\,(2\ln 2 - 1)\,, \tag{25}$$

a simple arithmetic mean over the $k-$profile. Using Eq. 16 and Eq. 22, and substituting the numerical value of $\bar{g}$ from Eq. 25, we get,

$$\begin{aligned} C_\mu &= \frac{8}{2\ln 2 - 1}\mathrm{Re_T}^{-2} = 0.1 \text{ and} \\ \frac{D}{C^2} &= \frac{8}{2\ln 2 - 1}\mathrm{Re_T}^{-1}. \end{aligned} \tag{26}$$

Doing the same for the equation for ϵ in Eq. 21 we get

$$4h + \xi h' + \frac{1}{\xi}\frac{\partial}{\partial \xi}\xi g' + \frac{C_{\epsilon 1}}{C}\left(f'\right)^2 - C_{\epsilon 2}\mathrm{Re_T}\frac{D}{C}\frac{h^2}{g} = 0.$$

We demand that

$$C_{\epsilon 2}\mathrm{Re_T}(D/C)(h/g) = 4. \tag{27}$$

Further, approximating $h/g \approx \bar{g}g/g$, we get

$$C_{\epsilon 2}\mathrm{Re_T}\frac{D}{C}\bar{g} = 4.$$

Combining with Eq. 22, we get

$$C_{\epsilon 2} = 2, \tag{28}$$

and the profile for ϵ is given by

$$\xi h' + \frac{1}{\xi}\frac{\partial}{\partial \xi}\left(\xi h'\right) + \frac{C_{\epsilon 1}}{C}\left(f'\right)^2 = 0.$$

Comparing with Eq. 23, we see that $h = C_{\epsilon 1} g$. Recall from Eq. 16 that $g^2/h = 1$ i.e., $h = g^2 \approx \bar{g}g$. Therefore,

$$\bar{g} \approx \frac{h}{g} = C_{\epsilon 1} = \frac{2\ln 2 - 1}{4C}, \tag{29}$$

where we use Eq. 25 for the numerical value of $\bar{g}$. To complete the estimates of $(C_\mu, C_{\epsilon 2}, C_{\epsilon 1})$, we need C. We use the Bradshaw assumption for turbulence shear stress [46], i.e., $\overline{u'v'} = 2/3 \times 0.45 \times k_s = 0.3k_s$. Also $\overline{u'v'} \approx \widehat{u_s}^2 f'/\mathrm{Re_T}$ where $f' = 0.5(f'_{max} + f'(\infty)) \approx 0.31$ (a simple mean over the entire $u-$profile). This gives:

$$\overline{u'v'} = \frac{0.31\widehat{u_s}^2}{\mathrm{Re_T}} = 0.3k_s.$$

Consequently

$$C = \frac{k_s}{\widehat{u_s}^2} = \frac{0.31\mathrm{Re_T}^{-1}}{0.3} = 0.072$$

and

$$C_{\epsilon 1} = \frac{2\ln 2 - 1}{4C} = 1.34. \tag{30}$$

Collating Eq. 26, Eq. 30 and Eq. 28, we get

$$C_\mu = 0.1,\ C_{\epsilon 2} = 2.0 \ \text{ and } \ C_{\epsilon 1} = 1.34 \tag{31}$$

These are the analytical values of $\mathbf{C}$ i.e., $\mathbf{C}_a$. They depend on the modeling assumptions in Eq. 16, 17, 22 and 27, whose validity is established by the predictive skill of $\mathbf{C}_a$. Eq. 16 is borrowed from the modeling of wakes; as stated in Ref. [14], scaling laws show that they are similar to the farfield in JIC interactions.

V. Results

We perform Bayesian calibration, following the method described in Sec. III.B and III.C, to construct four separate JPDFs using data from experiments described in Refs. [3, 5]. The JPDFs are marginalized and plotted in Fig. 5. The experiments ($M = 0.6, J = 10.2$), ($M = 0.7, J = 10.2$), ($M = 0.8, J = 10.2$) and ($M = 0.8, J = 16.7$) are plotted using solid, dashed, dotted, and long-dashed lines. The nominal values of $(C_\mu, C_{\epsilon 2}, C_{\epsilon 1})$ are plotted with a dashed vertical line and the analytical value $\mathbf{C}_a$ using a solid line. It is clear that the calibrated $C_{\epsilon 2}$ and analytical values of $C_{\epsilon 2}$ are far larger than the nominal value, and in line with the value obtained for axisymmetric jets [18]. Further, one could argue that the upper bound on $C_{\epsilon 2}$ could be increased to 2.5 (instead of 2.1), as used in Ref. [25]. Note that the tendency of the posterior densities to peak near the extremities of the parameter ranges are not an artifact of how we construct $\Pi_1(\mathbf{C})$ but rather that the parameter ranges in Eq. 4, taken from literature, may be too narrow. The PDFs for C_μ do not have the same consistency as the PDFs for $C_{\epsilon 2}$, though most of the peaks are at values larger than the nominal value. This conclusion is also supported by the analytical value, which is larger than the nominal one of 0.09. The PDFs for $C_{\epsilon 1}$ are all close to the nominal value of 1.44 with the exception of the ($M = 0.6, J = 10.2$) case. The plots of the model-data mismatch σ, which is in terms of the normalized streamwise velocity deficits and vertical velocities, show that the ($M = 0.6, J = 10.2$) calibration incurs the largest error; this will be investigated in detail later. The values of σ imply that a "pushed-forward posterior" run seeded by values of $(C_\mu, C_{\epsilon 2}, C_{\epsilon 1})$ sampled from the JPDFs plotted in Fig. 5 will not bracket the experimental measurements; instead they will need a model-data mismatch $\boldsymbol{\epsilon} \sim \mathcal{N}(0, \sigma^2)$, where σ is sampled from the PDF in Fig. 5. This aspect of the calibration for $(C_\mu, C_{\epsilon 2}, C_{\epsilon 1})$ was observed and explained in our previous paper where we developed the calibration method [9]; it is due to a combination of model-form error (the main component) and the approximation error of the statistical emulator for SIGMA CFD. The ($M = 0.7, J = 10.2$) experiment yields bimodal distributions for C_μ and $C_{\epsilon 1}$. In Fig. 6, we plot the JPDF, marginalized to two dimensions. We clearly see that C_μ and $C_{\epsilon 1}$ are correlated, achieving similar accuracies by compensating for each other.

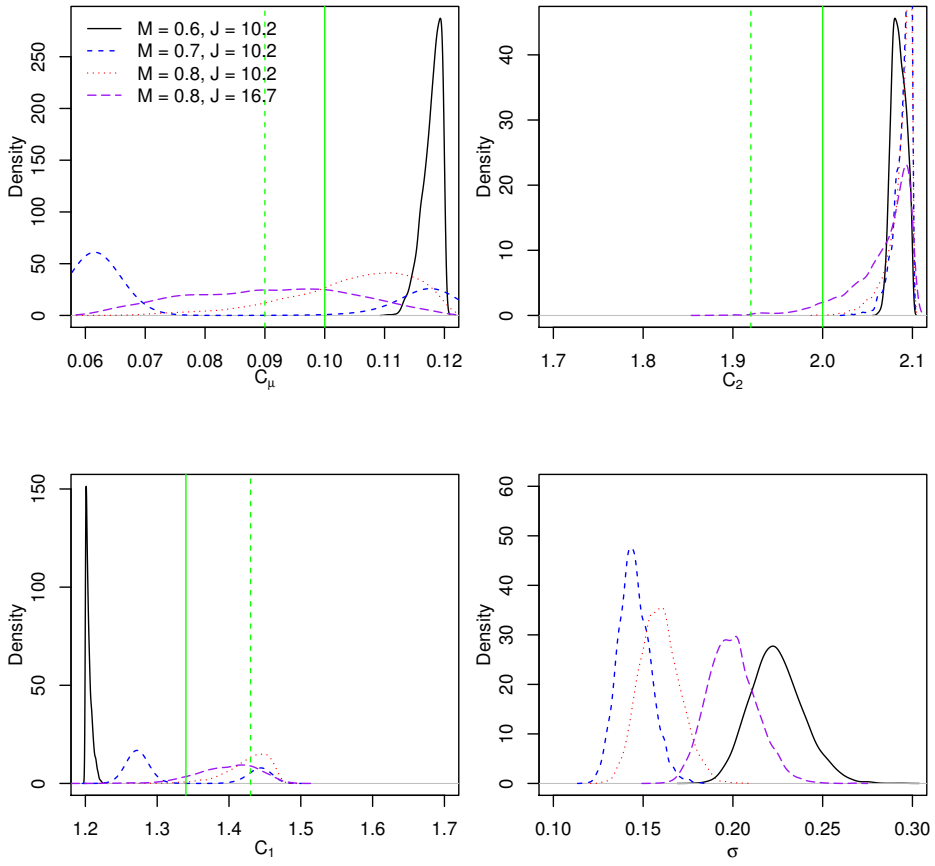

Fig. 5 Marginalized JPDFs of $(C_\mu, C_{\epsilon 2}, C_{\epsilon 1}, \sigma)$ obtained from the experimental data in Refs. [3]. The dashed vertical line is the nominal value of the $k-\epsilon$ constant and the solid vertical line is the analytically derived value (Eq. 31).

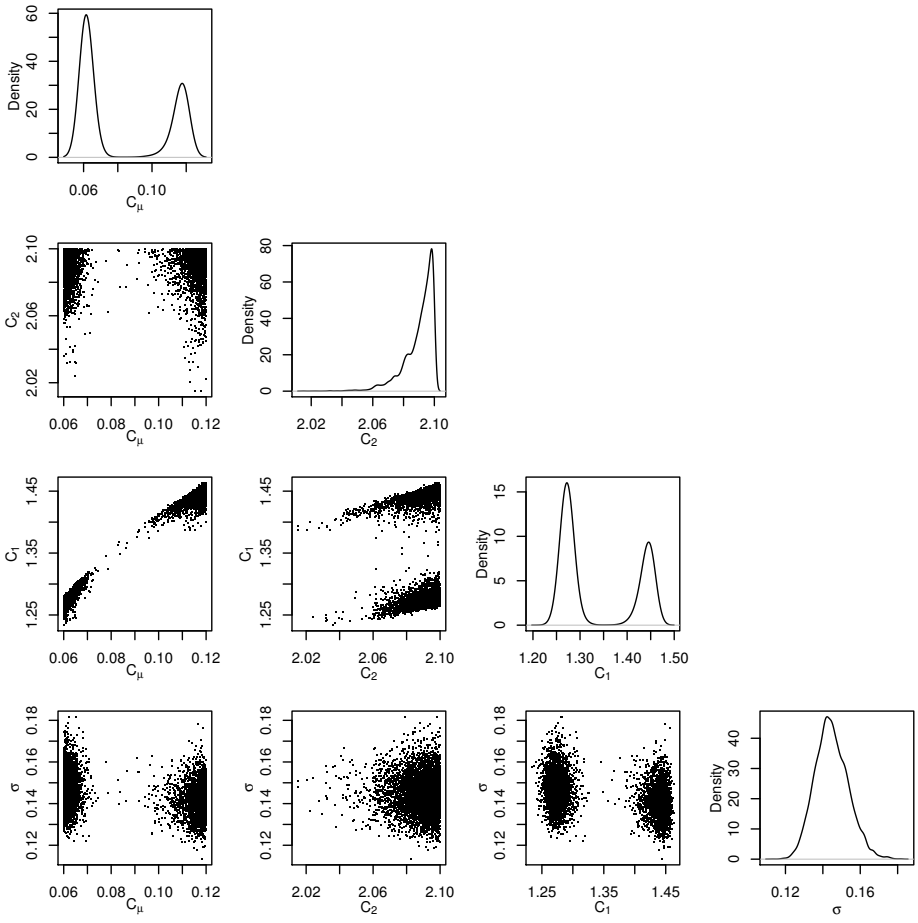

Fig. 6 The JPDF obtained from the $(M = 0.7, J = 10.2)$ experimental dataset, marginalized to two dimensions. The correlated nature of $(C_{\epsilon 1}, C_\mu)$ is clear.

Next, we check the predictive skill of the JPDFs plotted in Fig. 5. We do so using "pushed-forward posteriors" using 100 samples drawn from the JPDF (henceforth, the "ensemble"), as described in Sec. III.C. The variability in the prediction of mid-plane and cross-plane quantities is not much (below 10 %) as shown in our previous paper [9], and consequently we use the ensemble mean for visualizing mid-plane predictions. We also identify the $\mathbf{C}$ sample that produces predictions that match the measurements best; we call this $(C_\mu, C_{\epsilon 2}, C_{\epsilon 1})$ combination $\mathbf{C}_{opt}$. Since the variability of mid-plane predictions due to uncertainty in the inferred $(C_\mu, C_{\epsilon 2}, C_{\epsilon 1})$ is small, the ensemble mean prediction is quite close to the one produced by $\mathbf{C}_{opt}$.

In Fig. 7 we plot the streamwise velocity deficit u_{def} (top) and normalized vertical velocity v/U_∞ (bottom) at 3 streamwise locations $x/d_j = 21, 31.5$ and 42. Results are presented for the $(M = 0.8, J = 10.2)$ test case. The dotted line denotes predictions using $\mathbf{C}_{nom}$, the dashed line stands for $\mathbf{C}_a$, $\circ$ denote experimental measurements and the solid line is the ensemble mean prediction produced by the pushed-forward posterior. The vertical axis measures the normalized height y/d_j above the test-section floor. We see that the both u_{def} and v/U_∞ reach a maximum in the middle, coinciding with the center of the jet. Both decay to zero near the top of the test section. The vertical velocity is zero at the floor of the test section, whereas the streamwise velocity deficit decreases to near-zero as we depart the center of the jet and then increases as we progress into the boundary layer on the floor of the test section. Comparing the experimental measurements with the predictions using $\mathbf{C}_{nom}$ and the ensemble mean, we find the the JPDF improves the predictive skill of the simulations quite remarkably. What is surprising and reassuring is the degree of agreement achieved by the flowfield predicted using $\mathbf{C}_a$; further, the improvement holds across both the streamwise and vertical velocity fields as measured on the mid-plane at all three downstream locations. We do not have experimental measurements any closer to the jet exit to check the predictive skill of the JPDFs in the near-field.

The good agreement observed in Fig. 7 is expected since mid-plane velocities were the calibration variables. We check the ability of the JPDF for the $(M = 0.8, J = 10.2)$ test case to reproduce the vorticity field on the cross-plane; cross-plane measurements are not included in the calibration. In Fig. 8 (left) we plot contours of the vorticity field inside $\mathcal{W}$ produced by $\mathbf{C}_{nom}$ using solid lines. In the middle sub-figure, we plot the vorticity field predicted using $\mathbf{C}_a$. In the right sub-figure, we plot the vorticity field produced using $\mathbf{C}_{opt}$. Overlaid on all three sub-figures is the experimentally observed vorticity field plotted with the dash-dotted lines. It is clear, again, that there is a large improvement in the agreement between experimental and modeled vorticity field as we replace $\mathbf{C}_{nom}$ with $\mathbf{C}_{opt}$. Further, a similar degree of improvement is also observed when we use $\mathbf{C}_a$, in Fig. 8 (middle). In addition, the predictions using $\mathbf{C}_a$ and $\mathbf{C}_{opt}$ are very similar.

We next check the predictive accuracy of the JPDFs for the $(M = 0.8, J = 16.7)$ test case, using mid-plane u_{def} and v_{norm} as well as the cross-plane vorticity field as the comparison metrics. The plots for the mid-plane quantities are in Fig. 9. We see that the larger J causes problems for simulations when $\mathbf{C}_{nom}$ is used and the predictions of u_{def} and v_{norm} get progressively worse as we go downstream. In the Appendix, we check if predictions using $\mathbf{C}$ sampled

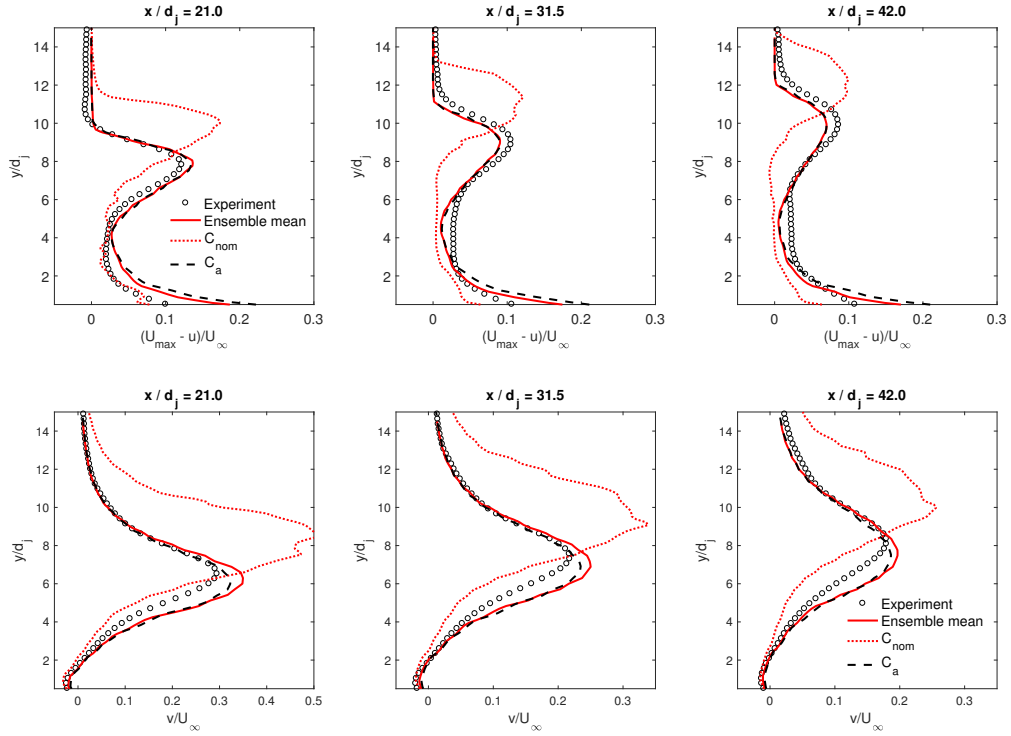

Fig. 7 Streamwise velocity deficit (above) and normalized vertical velocity (below) computed using $\mathbf{C}_{nom}$ and $\mathbf{C}_a$ compared with the ensemble mean from the "pushed-forward posterior" test and experimental measurements. Results are plotted for the $(M = 0.8, J = 10.2)$ test case, at three streamwise locations $(x/d_j = 21, 31.5$ and $42.0)$. We see that both $\mathbf{C}_a$ and $\mathbf{C}_{opt}$ provide better predictions than the nominal parameters $\mathbf{C}_{nom}$.

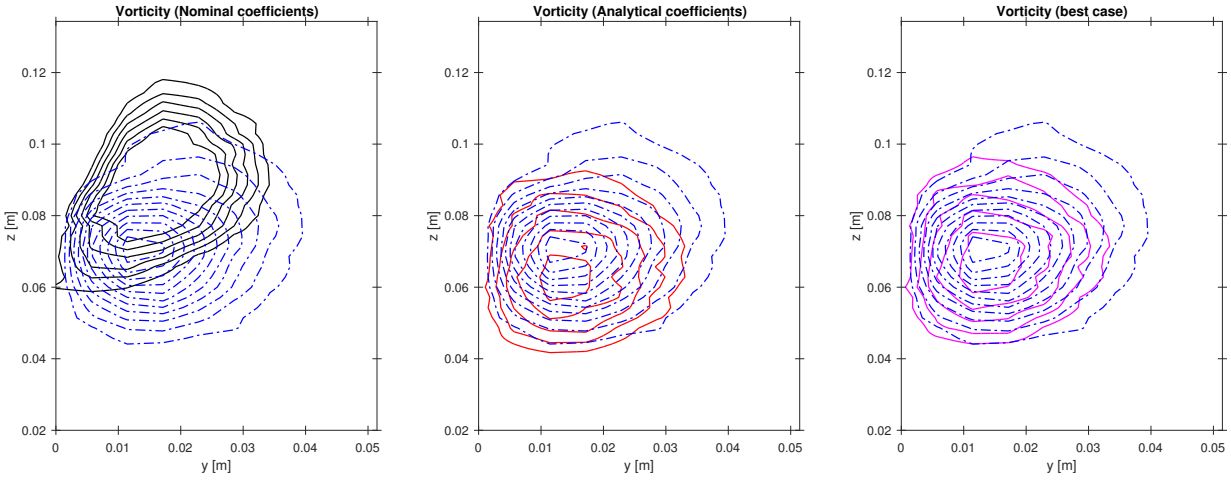

Fig. 8 Vorticity field on the cross-plane, as predicted using $\mathbf{C}_{nom}$ (left), $\mathbf{C}_a$ (middle) and $\mathbf{C}_{opt}$ (right) for the $(M = 0.8, J = 10.2)$ test case. The domain shown here is the window $\mathcal{W}$. Numerical predictions are plotted using a solid line $(-)$. Overlaid are experimental measurements of vorticity using a dash-dotted $(-.-)$ line. Again, $\mathbf{C}_{opt}$ and $\mathbf{C}_a$ improve predictions vis-á-vis the experimental measurements.

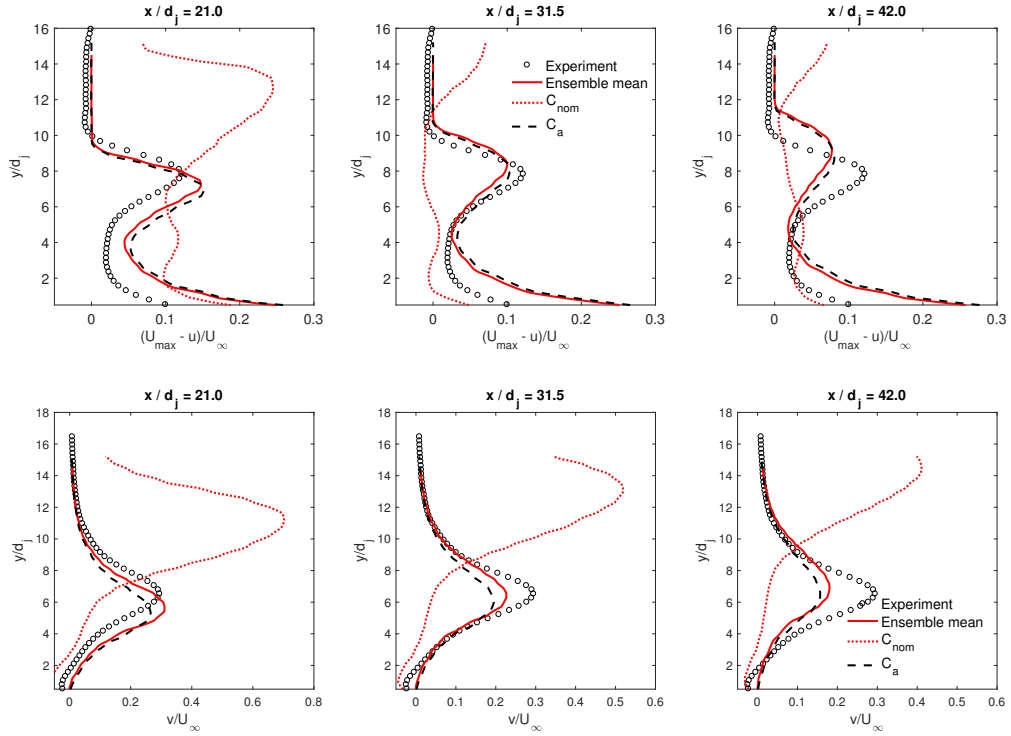

Fig. 9 Streamwise velocity deficit u_{def} (above) and normalized vertical velocity v_{norm} (below) computed using $\mathbf{C}_{nom}$ and $\mathbf{C}_a$ compared with the ensemble mean from the "pushed-forward posterior" simulations and experimental measurements. Results are plotted for the $(M = 0.8, J = 16.7)$ test case, at three streamwise locations $(x/d_j = 21, 31.5$ and $42.0)$. We see that both $\mathbf{C}_a$ and $\mathbf{C}_{opt}$ provide better predictions than the nominal parameters $\mathbf{C}_{nom}$. Also, the agreement between simulations and experimental measurements worsens downstream.

from the prior bracket observations. We see that they do, except for about 10 probes at the most downstream location at $x/d_j = 42.0$. The performance of the calibration is almost certainly affected by this shortcoming of the prior. Predictions using $\mathbf{C}_a$ and the ensemble mean are far better than the predictions with $\mathbf{C}_{nom}$. Further, the predictions with $\mathbf{C}_a$ agree closely with the ensemble mean of the "pushed-forward posterior" simulations, though the agreement worsens with increasing x/d_j. The numerical simulations underpredict both u_{def} and v_{norm}, and consequently a weaker CVP. In Fig. 10, we plot the vorticity field inside $\mathcal{W}$ as predicted using $\mathbf{C}_{nom}$ (left sub-figure), $\mathbf{C}_a$ (middle sub-figure) and $\mathbf{C}_{opt}$ (right sub-figure). Predictions using the nominal values of $\mathbf{C}$ do not even reside inside $\mathcal{W}$, and by that token, $\mathbf{C}_a$ and $\mathbf{C}_{opt}$ perform far better. However, as Fig. 9 shows, the agreement between modeled and experimental velocity fields mid-plane degrades as as we proceed downstream, and consequently, comparison between the measured and predicted vorticity fields on the crossplane (situated at $x/d_j = 33.76$) is not as good as the one observed for the $(M = 0.8, J = 10.2)$ case (compare Fig. 10 versus Fig. 8; the simulated vortex sits below the experimental one for $J = 16.7$). This is particularly true for the predictions using $\mathbf{C}_a$.

In Fig. 11 we plot the mid-plane predictions using $\mathbf{C}_{nom}$ and the ensemble mean from "pushed-forward posterior" simulations from the JPDF for the $(M = 0.7, J = 10.2)$ test case. We see that predictions are quite close to the

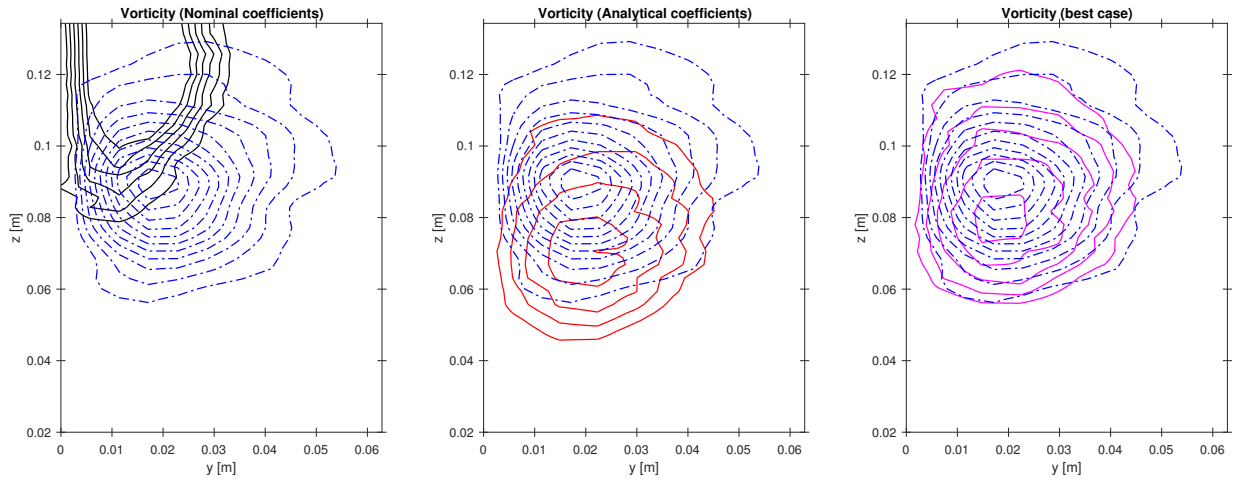

Fig. 10 Vorticity on the cross-plane as predicted using $\mathbf{C}_{nom}$ (left), $\mathbf{C}_a$ (middle) and $\mathbf{C}_{opt}$ (right) for the $(M = 0.8, J = 16.7)$ test case. The domain shown here is the window $\mathcal{W}$. Numerical predictions are plotted using a solid line $(-)$. Overlaid are experimental measurements of vorticity using a dash-dotted $(-.-)$ line. $\mathbf{C}_{opt}$ and $\mathbf{C}_a$ have a better agreement with measurements than the prediction using $\mathbf{C}_{nom}$, which does not even lie inside $\mathcal{W}$.

experimental measurements, and are a large improvement over predictions using $\mathbf{C}_{nom}$. This is particularly true for the vertical velocity. In Fig. 12, we plot the vorticity field on the cross-plane inside $\mathcal{W}$, as predicted using $\mathbf{C}_a$ and $\mathbf{C}_{opt}$. We see that they agree quite well. No experimental measurements were taken on the cross-plane for this test case, and so we do not know the degree to which the calibrated and analytical vorticity fields improved on the one generated by $\mathbf{C}_{nom}$; consequently, we have omitted that plot.

A. Discussion

The mid-plane results provided above in Figs. 7, 9 and 11 show that the calibrated predictions (i.e., ensemble mean of the "pushed-forward posterior" predictions, seeded using the JPDFs in Fig. 5) invariably have a better agreement with experimental measurements than predictions using the nominal value of $k-\epsilon$ constants $\mathbf{C}_{nom}$. This is perhaps not very surprising, given that mid-plane measurements *are* the calibration variables. What is surprising is the degree to which predictions using the *analytical* values of $\mathbf{C}$ i.e., $\mathbf{C}_a$, follow the calibrated ensemble means in all three test cases analyzed above. As mentioned before, the JPDFs almost certainly compensate for some RANS model-form errors; however, given the close agreement with $\mathbf{C}_a$ predictions, they are probably not excessive. $\mathbf{C}_a$, being derived analytically, with no fitting to the datasets used in this paper, is free of any conflation between parametric and model-form uncertainties. Further, had the compensation of model-form errors by the JPDFs been large, the residual data - model mismatch σ would have been small. As the PDFs for σ in Fig. 5 show, this is not the case.

The ability of the JPDFs to reproduce the measured flowfield on the cross-plane is somewhat mixed. We checked this by identifying an "optimal" $\mathbf{C} = \mathbf{C}_{opt}$ from the "pushed-forward posterior" simulations, and comparing its cross-

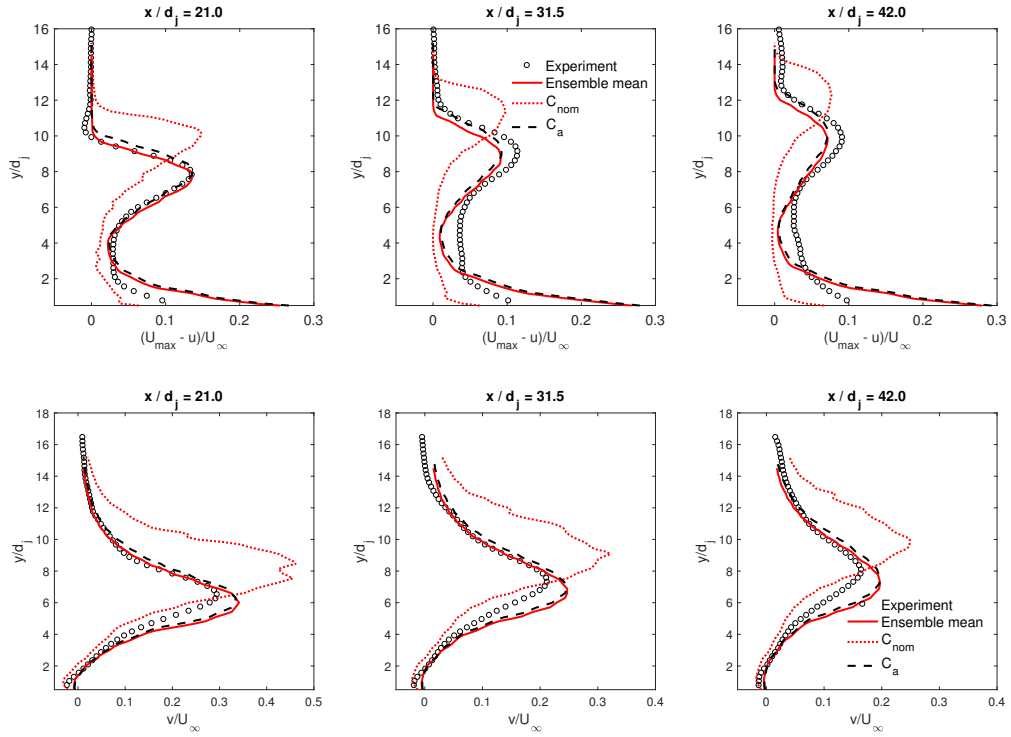

Fig. 11 Streamwise velocity deficit u_{def} (above) and normalized vertical velocity v_{norm} (below) computed using $\mathbf{C}_{nom}$ and $\mathbf{C}_a$ compared with the ensemble mean from the "pushed-forward posterior" simulations and experimental measurements. Results are plotted for the $(M = 0.7, J = 10.2)$ test case, at three streamwise locations $(x/d_j = 21, 31.5$ and $42.0)$. We see that both $\mathbf{C}_a$ and $\mathbf{C}_{opt}$ provide better predictions than the nominal parameters $\mathbf{C}_{nom}$.

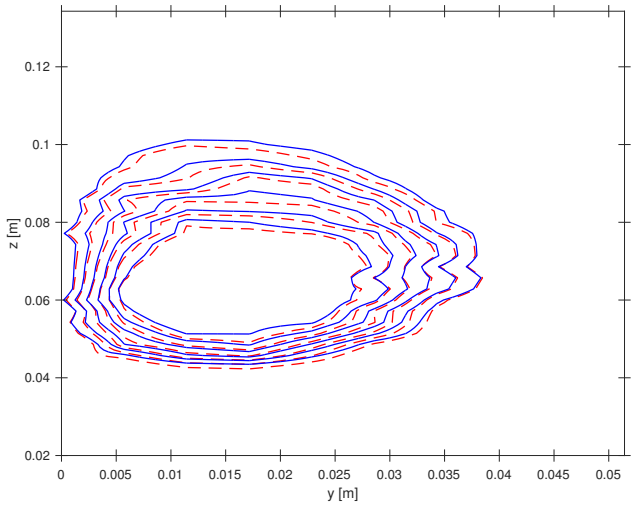

Fig. 12 Contour plots of the vorticity field generated on the cross-plane using $\mathbf{C}_{opt}$ (solid lines, $-$) and $\mathbf{C}_a$ (dashed line, $--$) for the $(M = 0.7, J = 10.2)$ test case. We do not have experimental measurements for this test case.

plane vorticity predictions against experimental data. Note that a different $\mathbf{C}_{opt}$ is obtained for each test case; these are tabulated in Table 1. Calibration invariably provided a better prediction than $\mathbf{C}_{nom}$, and for the $(M = 0.8, J = 10.2)$ test case, the match with experimental data was quite impressive. The agreement was somewhat less impressive in the $(M = 0.8, J = 16.7)$ test case (see Fig. 10), which may be partially due to the overly-restrictive prior (see the Appendix for details). In all cases, predictions using $\mathbf{C}_a$ closely tracked the calibrated predictions.

It is clear, then, that the JPDFs could be improved. In Ref. [9], where we developed the Bayesian calibration technique, we had obtained a JPDF for $\mathbf{C}$ using vorticity measurements on the cross-plane using the $(M = 0.8, J = 10.2)$ test case. We had also obtained an "optimal" value of $\mathbf{C}$ using a genetic algorithm, which we tabulate below (Table 1) as $\mathbf{C}^{(ga)}$. The dominant flow feature in the JIC interaction is the CVP and calibrating to its direct measurements provided us with a robust JPDF. Being able to reproduce the CVP in the correct position and with the correct circulation automatically led to a flowfield that agreed with measurements on the mid-plane. It was also compared, with somewhat less agreement, to measurements from the $(M = 0.8, J = 16.7)$ and $(M = 0.7, J = 10.2)$ test cases. However, it was not optimized to those particular test cases, and one could never be sure whether any discrepancies between predictions developed using $\mathbf{C}^{(ga)}$ and $\mathbf{C}_a$ were due to compensations of model-form errors, the approximations adopted to obtain $\mathbf{C}_a$ or the shortcomings of the JPDF due to limited and noisy measurements. This led to our decision to calibrate to each of the test cases, and the necessity of using mid-plane measurements (since cross-plane measurements were only available for $M = 0.8$ test cases). The mid-plane measurements are less informative of the CVP than the cross-plane ones, and hence our mixed results in reproducing cross-plane vorticity fields, post-calibration.

Note that in this study we do not test the generalizability of a JPDF developed for a (M, J) to other (M, J) combinations. As mentioned above, generalization was studied in Ref. [9], with encouraging results. It led us to believe that a modification of the JPDF for the $(M = 0.8, J = 10.2)$ could be predictive for other conditions, and consequently this study. Also, note that in Figs. 7, 9 and 11 we plot the ensemble mean of the "pushed-forward posterior" simulations, without any measure of the variability in them. This is because the variability is small and will not help bracket the observations; as shown in Ref. [9], one needs to include the effect of σ to successfully do so. This implies that, post-calibration, the parametric uncertainty is far smaller than σ, a composite of model-form, measurement and surrogate modeling errors, and any further improvement in predictive skill is dependent on reducing σ, e.g., via reducing model-form errors.

Fig. 5 shows two curious features - the estimate of $C_{\epsilon 1}$ obtained for the $(M = 0.6, J = 10.2)$ case is quite different from the other ones and the data - model mismatch σ is the largest of all the test cases considered. We investigate this further. In Fig. 13, we plot u_{def} and v_{norm} predictions due to $\mathbf{C}_a$, $\mathbf{C}_{nom}$ and the ensemble mean of "pushed-forward posterior" simulations, and compare them with experimental observations. As in Figs. 7, 9 and 11, we see a peak in u_{def} in the middle of the domain (the jet core) and a large value of the same in the boundary layer at the bottom of the test section. In between the jet core and the floor of the test section, u_{def} should have decreased to a small number

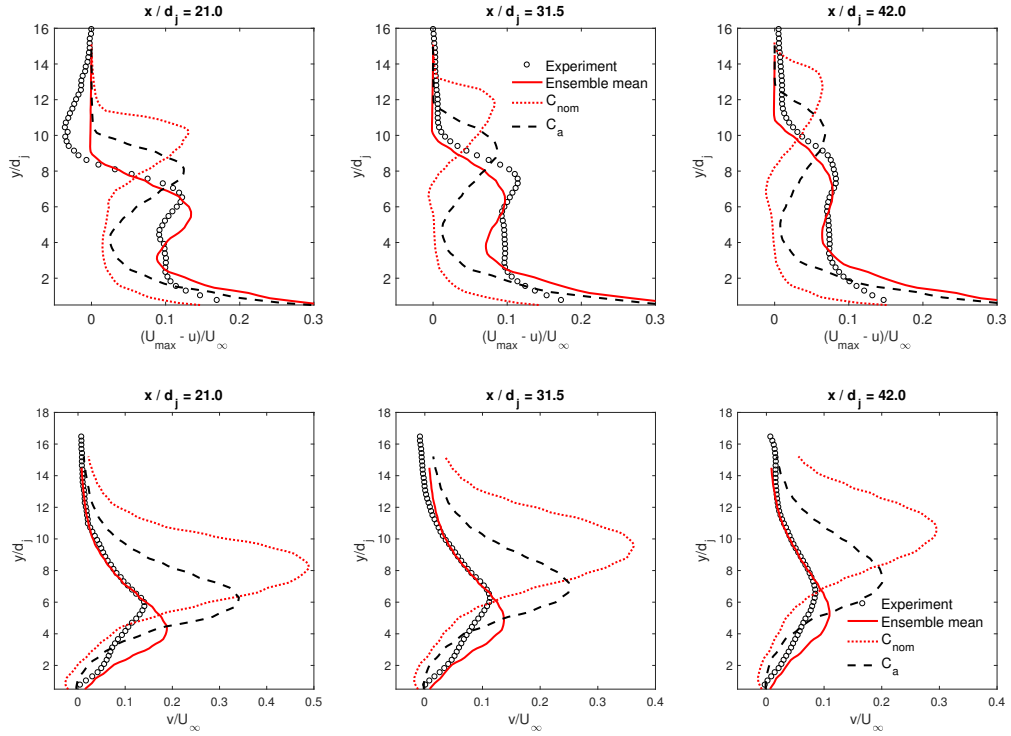

Fig. 13 Streamwise velocity deficit u_{def} (above) and normalized vertical velocity v_{norm} (below) computed using $\mathbf{C}_{nom}$ and $\mathbf{C}_a$ compared with the ensemble mean from the "pushed-forward posterior" simulations and experimental measurements. Results are plotted for the $(M = 0.6, J = 16.7)$ test case, at three streamwise locations $(x/d_j = 21, 31.5$ and $42.0)$. We see that both $\mathbf{C}_a$ and $\mathbf{C}_{opt}$ provide better predictions than the nominal parameters $\mathbf{C}_{nom}$, though their agreement is not as good as those seen in Fig. 11, 7 and 9.

outside the jet; this is seen in Figs. 7, 9 and 11 for all the test cases. As is clear in Fig. 13, the measurements do not show this trend for the $(M = 0.6, J = 10.2)$ case, though predictions using $\mathbf{C}_{nom}$ and $\mathbf{C}_a$ do. We cannot explain this aspect of the experimental measurements, but we do calibrate to it. This could be the explanation behind the "anomalous" PDF for $C_{\epsilon 1}$. Despite the calibration, the $k-\epsilon$ RANS model does not reproduce the flowfield well (as seen in Fig. 13) leading to large σ in Fig. 5.

Table 1 contains a list of optimal $\mathbf{C}$ that we have identified in this study, as well as from previous Bayesian calibrations using experimental data employed in this study. From Fig. 5 and Table 1, we that $\mathbf{C}_a$ is close to the calibrated values, reproduces mid-plane measurements well, and is far more predictive than $\mathbf{C}_{nom}$ in all cases (mid- and cross-plane predictions). Further, $\mathbf{C}_a$ respects the trends seen in the JPDFs in Fig. 5 - C_μ and $C_{\epsilon 2}$ are higher than their nominal counterparts whereas $C_{\epsilon 1}$ is similar to the nominal value. In addition, the analytical model from which $\mathbf{C}_a$ is derived has been used to predict the trajectory of the jet [13]. These analytical predictions have been compared to $k-\epsilon$ predictions using $\mathbf{C}_a$, $\mathbf{C}_{nom}$ and experimental data (the $M = (0.6, 0.7, 0.8)$, $J = 10.2$ test cases). In all three cases, both $\mathbf{C}_a$ and the analytical trajectory agreed better with experimental data than $k-\epsilon$ RANS predictions using $\mathbf{C}_{nom}$. It is thus clear that the analytical model developed in Sec. IV embodies the essential physics in JIC interactions,

is far more predictive than $\mathbf{C}_{nom}$ and is close to the calibrated model parameters developed in this study. It could serve an alternative to $\mathbf{C}_{nom}$ for $k-\epsilon$ RANS simulations of compressible JIC interactions.

Table 1 Values of $\mathbf{C}_{opt}$ obtained for the test cases in this study. $\mathbf{C}^{(ga)}$ is an estimate from Ref. [9] and $\mathbf{C}_a$ was derived in this study.

Test case	Optimal $(C_\mu, C_{\epsilon 2}, C_{\epsilon 1})$
$(M = 0.8, J = 10.2)$ $\mathbf{C}_{opt}^{(ga)}$, from Ref. [9]	$\{0.105, 2.099, 1.42\}$
$(M = 0.8, J = 10.2)$	$\{0.11, 2.095, 1.44\}$
$(M = 0.7, J = 10.2)$	$\{0.11, 2.09, 1.46\}$
$(M = 0.8, J = 16.7)$	$\{0.11, 2.04, 1.45\}$
$(M = 0.6, J = 10.2)$	$\{0.117, 2.09, 1.2\}$
$\mathbf{C}_a$	$\{0.1, 2.0, 1.34\}$

VI. Conclusions

Despite their shortcomings, two-equation RANS models e.g., $k-\epsilon$ and $k-\omega$ models, are the backbone of engineering aerodynamic simulations. The nominal values of RANS parameters $\mathbf{C}_{nom}$ are not predictive and they are often tuned. $k-\epsilon$ RANS models have been shown to be not predictive for compressible JIC simulations, and in view of their engineering relevance, it is clear that a replacement for $\mathbf{C}_{nom}$ would be useful. It is less clear what that replacement might be, and whether it would hold across a range of crossflow Mach numbers and jet strengths. We have attempted to investigate the problem rigorously, and may have found a replacement. Note that this rigor does not endow our estimate of $k-\epsilon$ constants with any degree of universality across types of flows - it has been shown to be predictive for compressible JIC simulations only. Its predictive skill for other classes of flows has not been tested.

In one of our previous papers on this topic [9], we developed a Bayesian method to compute JPDFs of $k-\epsilon$ constants. The JPDF captures the uncertainty in the inferred $k-\epsilon$ constants. The decision to treat the $k-\epsilon$ constants as random variables and compute their JPDF from data was deliberate. We were mindful of the approximation errors in RANS, as well as the sparsity of experimental compressible JIC datasets that contained measurements of velocity (as opposed to just the trajectory of the jet), neither of which are conducive to parameter estimation with a great deal of certainty. As discussed in Sec. I, this work led us to believe that parametric uncertainties, rather than model-form errors, might be responsible for the poor predictive skill of $k-\epsilon$ RANS for JIC interactions. Our second paper [11] investigated whether the inability of RANS models with linear eddy viscosities to model anisotropy in turbulence could account for the poor predictive power of RANS for JIC interactions. We found that nonlinear eddy viscosity models too had to be calibrated to data, and, post-calibration, were not vastly more predictive than linear eddy viscosities. This study reinforced our belief that a modification of $\mathbf{C}_{nom}$ would be sufficient to improve RANS JIC simulations.

Both the calibration studies mentioned above ran the risk of the inferred JPDFs for $k-\epsilon$ constants could compensate for model-form errors. However, if JPDFs were developed for individual experiments (and thus compensated for model-

form errors to differing degrees), any points of similarity between them could indicate how $\mathbf{C}_{nom}$ would have to change to be predictive. These JPDFs are plotted in Fig. 5 and show that (1) $C_{\epsilon 2}$ and C_μ would have to be larger than their nominal counterparts and (2) $C_{\epsilon 1}$ could remain unchanged. We also developed an analytical model of an incompressible JIC interaction and obtained $k-\epsilon$ constants' estimates. Since this involved no model fitting to our datasets, the analytical model is free of any compensation of model-form errors. We found that these "analytical" $k-\epsilon$ parameters obey the trends seen in the JPDFs. Further flowfields predicted using the JPDFs and the analytical $k-\epsilon$ constants are similar, and in turn are closer to measurements than predictions with $\mathbf{C}_{nom}$. These outcomes lead us to believe that the effect of model-form errors on the JPDFs are small, that the predictive skill of $\mathbf{C}_a$ would carry over to (M, J) combinations for which we do not have measurements and $\mathbf{C}_a$ would be preferable to $\mathbf{C}_{nom}$ for JIC simulations.

Having calibrated $k-\epsilon$ constants, any residual model - data mismatch is largely due to model-form errors. This manifests itself most prominently as the disagreement between modeled and measured turbulent stresses, as we illustrated in one of our previous papers [9]. The analytical model is entirely derived using mean flow quantities rather than turbulent stresses and thus contributes nothing to rectify this shortcoming. Consequently, further improvements of the calibrated $k-\epsilon$ model for JIC simulations will require augmentation of the equations to reduce approximation errors, e.g., by employing eddy viscosity models that accommodate anisotropy. Methods and approaches that might help in this regard were reviewed in Sec. II. Specifically, the method developed by Ling et al [36] may serve as an attractive starting point as it has already been applied successfully in incompressible jet-in-crossflow interactions [38, 48].

Acknowledgments

This work was supported by Sandia National Laboratories' Advanced Scientific Computing (ASC) Verification and Validation program. Sandia National Laboratories is a multimission laboratory managed and operated by National Technology and Engineering Solutions of Sandia LLC, a wholly owned subsidiary of Honeywell International Inc. for the U.S. Department of Energy's National Nuclear Security Administration under contract DE-NA0003525. This paper describes objective technical results and analysis. Any subjective views or opinions that might be expressed in the paper do not necessarily represent the views of the U.S. Department of Energy or the United States Government.

References

[1] Mahesh, K., "The interaction of jets with crossflows," *Annual Reviews of Fluid Mechanics*, Vol. 45, 2013, pp. 379–407. doi:10.1146/annurev-fluid-120710-101115.

[2] Peterson, C. W., Wolfe, W. P., and Payne, J. L., "Experiments and computations of roll torque induced by vortex-fin interaction," *42nd AIAA Aerospace Sciences Meeting and Exhibit, Reno, NV (AIAA 2004-1069)*, 2004. doi:10.2514/6.2004-1069.

[3] Beresh, S. J., Henfling, J. F., Erven, R. J., and Spillers, R. W., "Penetration of a transverse supersonic jet into a subsonic compressible crossflow," *AIAA Journal*, Vol. 43, No. 2, 2005, pp. 379–389. doi:10.2514/1.9919.

[4] Beresh, S. J., Henfling, J. F., Erven, R. J., and Spillers, R. W., "Turbulent characteristics of a transverse supersonic jet in a subsonic compressible crossflow," *AIAA Journal*, Vol. 43, No. 11, 2005, pp. 2385–2394. doi:10.2514/1.14575.

[5] Beresh, S. J., Henfling, J. F., Erven, R. J., and Spillers, R. W., "Crossplane velocimetry of a transverse supersonic jet in a transonic crossflow," *AIAA Journal*, Vol. 44, No. 12, 2006, pp. 3051–3061. doi:10.2514/1.22311.

[6] Beresh, S. J., Heineck, J. T., Walker, S. M., Shairer, E. T., and Yaste, D. M., "Vortex structure produced by a laterally inclined supersonic jet in transonic crossflow," *Journal of Propulsion and Power*, Vol. 23, No. 2, 2007, pp. 353–363. doi: 10.2514/1.25444.

[7] Beresh, S. J., Heineck, J. T., Walker, S. M., Schairer, E. T., and Yaste, D. M., "Planar velocimetry of jet/fin interaction on a full-scale flight vehicle configuration," *AIAA Journal*, Vol. 45, No. 8, 2007, pp. 1827–1840. doi:10.2514/1.26485.

[8] Arunajatesan, S., "Evaluation of two-equations RANS models for simulation of jet-in-crossflow problems," *50th AIAA Aerospace Sciences Meeting including the New Horizons Forum and Aerospace Exposition, Aerospace Sciences Meetings, Nashville, TN (AIAA 2012-1199)*, 2012. doi:10.2514/6.2012-1199.

[9] Ray, J., Lefantzi, S., Arunajatesan, S., and Dechant, L., "Bayesian parameter estimation of a k-epsilon model for accurate jet-in-crossflow simulations," *American Institute of Aeronautics and Astronautics Journal*, Vol. 54, No. 8, 2016, pp. 2432–2448. doi:10.2514/1.J054758.

[10] Wilcox, D. C., *Turbulence Modeling for CFD*, D C W Industries, 1998.

[11] Ray, J., Lefantzi, S., Arunajatesan, S., and DeChant, L., "Learning an eddy viscosity model using shrinkage and Bayesian calibration: A jet-in-crossflow case study," *ASME Journal of Risk Uncertainty Part B*, Vol. 4, No. 1, 2017, pp. 011001–011001–10. doi:10.1115/1.4037557.

[12] Ray, J., Lefantzi, S., Arunajatesan, S., and DeChant, L. J., "Robust Bayesian calibration of a RANS model for jet-in-crossflow simulations," *8th AIAA Theoretical Fluid Mechanics Conference, AIAA AVIATION Forum (AIAA 2017-4166)*, 2017. doi: 10.2514/6.2017-4166.

[13] DeChant, L. J., Ray, J., Lefantzi, S., Ling, J., and Arunajatesan, S., "$K-\epsilon$ turbulence model parameter estimates using an approximate self-similar jet-in-crossflow solution," *8th AIAA Theoretical Fluid Mechanics Conference, AIAA AVIATION Forum, (AIAA 2017-4167)*, 2017. doi:10.2514/6.2017-4167.

[14] Hasselbrink, E. F., and Mungal, M. G., "Transverse jets and jet flames. Part 1. Scaling laws for strong transverse jets," *Journal of Fluid Mechanics*, Vol. 443, 2001, p. 1–25. doi:10.1017/S0022112001005146.

[15] Broadwell, J. E., and Breidenthal, R. E., "Structure and mixing of a transverse jet in incompressible flow," *Journal of Fluid Mechanics*, Vol. 148, 1984, p. 405–412. doi:10.1017/S0022112084002408.

[16] Karagozian, A. R., "An analytical model for the vorticity associated with a transverse jet," *AIAA Journal*, Vol. 24, No. 3, 1986, pp. 429–436. doi:10.2514/3.9285.

[17] Heister, S., and Karagozian, A., "Vortex modeling of gaseous jets in a compressible crossflow," *24th Joint Propulsion Conference, Joint Propulsion Conferences*, 1988. doi:10.2514/6.1988-3270.

[18] Thies, A. T., and Tam, C. K. W., "Computation of turbulent axisymmetric and nonaxisymmetric jet flows using the $k-\epsilon$ model," *AIAA Journal*, Vol. 34, No. 2, 1996, pp. 309–316. doi:10.2514/3.13065.

[19] Shirzadi, M., Mirzaei, P. A., and Naghashzadegan, M., "Improvement of $k-\epsilon$ turbulence model for CFD simulation of atmospheric boundary layer around a high-rise building using stochastic optimization and Monte Carlo Sampling technique," *Journal of Wind Engineering and Industrial Aerodynamics*, Vol. 171, No. Supplement C, 2017, pp. 366 – 379. doi:10.1016/j.jweia.2017.10.005.

[20] Pope, S. B., "An explanation of the turbulent round-jet/plane-jet anomaly," *AIAA Journal*, Vol. 16, No. 3, 1978, pp. 279–281. doi:10.2514/3.7521.

[21] Sarkar, S., and Lakshmanan, B., "Application of a Reynolds stress turbulence model to the compressible shear layer," *AIAA Journal*, Vol. 29, No. 5, 1991, pp. 743–749. doi:10.2514/3.10649.

[22] Cheung, S. H., Oliver, T. A., E. E. Prudencio, S. P., and Moser, R. D., "Bayesian uncertainty analysis with applications to turbulence modeling," *Reliability Engineering and System Safety*, Vol. 96, 2011, pp. 1137–1149. doi:10.1016/j.ress.2010.09.013.

[23] Edeling, W. N., Cinnella, P., Dwight, R. P., and Bijl, H., "Bayesian estimates of parameter variability in $k-\epsilon$ turbulence model," *Journal of Computational Physics*, Vol. 258, 2014, pp. 73–94. doi:10.1016/j.jcp.2013.10.027.

[24] Edeling, W. N., Cinnella, P., and Dwight, R. P., "Predictive RANS simulations via Bayesian Model-Scenario Averaging," *Journal of Computational Physics*, Vol. 275, 2014, pp. 65–91. doi:10.1016/j.jcp.2014.06.052.

[25] Guillas, S., Glover, N., and Malki-Epshtein, L., "Bayesian calibration of the constants of the $k-\epsilon$ turbulence model for a CFD model of street canyon flow," *Computer Methods in Applied Mechanics and Engineering*, Vol. 279, 2014, pp. 536–553. doi:10.1016/j.cma.2014.06.008.

[26] Zhang, J., and Fu, S., "An efficient Bayesian uncertainty quantification approach with application to $k-\epsilon-\gamma$ transition modeling," *Computers & Fluids*, Vol. 161, No. Supplement C, 2018, pp. 211 – 224. doi:10.1016/j.compfluid.2017.11.007.

[27] Kato, H., Ishiko, K., and Yoshizawa, A., "Optimization of parameter values in the turbulence model aided by data assimilation," *AIAA Journal*, Vol. 54, No. 5, 2016, pp. 1512–1523. doi:10.2514/1.J054109.

[28] Dow, E., and Wang, Q., "Quantification of structural uncertainties in the $k-\omega$ turbulence model," *52nd AIAA/ASME/ASCE/AHS/ASC Structures, Structural Dynamics and Materials Conference, Structures, Structural Dynamics, and Materials and Co-located Conferences*, 2011. doi:10.2514/6.2011-1762.

[29] Weatheritt, J., and Sandberg, R., "A novel evolutionary algorithm applied to algebraic modifications of the RANS stress–strain relationship," *Journal of Computational Physics*, Vol. 325, No. Supplement C, 2016, pp. 22 – 37. doi:10.1016/j.jcp.2016.08.015.

[30] Gorlé, C., and Iaccarino, G., "A framework for epistemic uncertainty quantification of turbulent scalar flux models for Reynolds-averaged Navier-Stokes simulations," *Physics of Fluids*, Vol. 25, 2013, p. 055105. doi:10.1063/1.4807067.

[31] Wu, J.-L., Wang, J.-X., and Xiao, H., "A Bayesian calibration–prediction method for reducing model-form uncertainties with application in RANS simulations," *Flow, Turbulence and Combustion*, Vol. 97, No. 3, 2016, pp. 761–786. doi:10.1007/s10494-016-9725-6.

[32] Wang, J.-X., Wu, J.-L., and Xiao, H., "Physics-informed machine learning approach for reconstructing Reynolds stress modeling discrepancies based on DNS data," *Physical Review Fluids*, Vol. 2, 2017, p. 034603. doi:10.1103/PhysRevFluids.2.034603.

[33] Parish, E. J., and Duraisamy, K., "A paradigm for data-driven predictive modeling using field inversion and machine learning," *Journal of Computational Physics*, Vol. 305, No. Supplement C, 2016, pp. 758 – 774. doi:10.1016/j.jcp.2015.11.012.

[34] Singh, A. P., Medida, S., and Duraisamy, K., "Machine-learning-augmented predictive modeling of turbulent separated flows over airfoils," *AIAA Journal*, Vol. 55, No. 7, 2017, pp. 2215–2227. doi:10.2514/1.J055595.

[35] Edeling, W. N., Iaccarino, G., and Cinnella, P., "Data-free and data-driven RANS predictions with quantified uncertainty," *Flow, Turbulence and Combustion*, 2017. doi:10.1007/s10494-017-9870-6.

[36] Ling, J., Kurzawski, A., and Templeton, J., "Reynolds averaged turbulence modelling using deep neural networks with embedded invariance," *Journal of Fluid Mechanics*, Vol. 807, 2016, pp. 155–166. doi:10.1017/jfm.2016.615.

[37] Barone, M. F., Ling, J., Chowdhary, K., Davis, W., and Fike, J., "Machine learning models of errors in Large Eddy Simulation predictions of surface pressure fluctuations," *47th AIAA Fluid Dynamics Conference, AIAA AVIATION Forum (AIAA 2017-3979)*, 2017. doi:10.2514/6.2017-3979.

[38] Milani, P. M., Ling, J., Saez-Mischlich, G., Bodart, J., and Eaton, J. K., "A machine learning approach for determining the turbulent diffusivity in film cooling flows," *ASME Journal of Turbomachinery*, Vol. 140, No. 2, 2017, pp. 021006–021006–8. doi:10.1115/1.4038275.

[39] Brinckman, K. W., Calhoon, W. H., and Dash, S. M., "Scalar fluctuation modeling for high-speed aeropropulsive flows," *AIAA Journal*, Vol. 45, No. 5, 2007, pp. 1036–1046. doi:10.2514/1.21075.

[40] Haario, H., Laine, M., Mira, A., and Saksman, E., "DRAM-Efficient adaptive MCMC," *Statistics and Computing*, Vol. 16, No. 4, 2006, pp. 339–354. doi:10.1007/s11222-006-9438-0.

[41] Raftery, A., and Lewis, S. M., "Implementing MCMC," *Markov Chain Monte Carlo in Practice*, edited by W. R. Gilks, S. Richardson, and D. J. Spiegelhalter, Chapman and Hall, 1996, pp. 115–130.

[42] R Core Team, *R: A Language and Environment for Statistical Computing*, R Foundation for Statistical Computing, Vienna, Austria, 2012. http://www.R-project.org/.

[43] Soetaert, K., and Petzoldt, T., "Inverse modelling, sensitivity and Monte Carlo analysis in R using package FME," *Journal of Statistical Software*, Vol. 33, No. 3, 2010, pp. 1–28. http://www.jstatsoft.org/v33/i03/.

[44] Warnes, G. R., and with contributions by Robert Burrows, *mcgibbsit: Warnes and Raftery's MCGibbsit MCMC diagnostic*, 2011. http://CRAN.R-project.org/package=mcgibbsit.

[45] Silverman, B. W., *Density Estimation for Statistics and Data Analysis*, Chapman and Hall, 1986.

[46] Pope, S. B., *Turbulent Flows*, Cambridge University Press, 2009.

[47] Tennekes, H., and Lumley, J., *A first course in turbulence*, MIT Press, Cambridge, MA, 1987, pp. 104–145.

[48] Ling, J., Ruiz, A., Lacaze, G., and Oefelein, J., "Uncertainty analysis and data-driven model advances for a jet-in-crossflow," *ASME Journal of Turbomachinery*, Vol. 139, No. 2, 2016, pp. 021008–021008–9. doi:10.1115/1.4034556.

A. Checking the prior for $(M = 0.8, J = 16.7)$ test case

In this appendix we investigate the cause of the poor predictions of the mid-plane velocities seen in Fig. 9. We check if the prior $\Pi_1(\mathbf{C})$ can bracket the observations for the $(M = 0.8, J = 16.7)$ test case. We pick 100 random samples of $\mathbf{C}$ from the prior and simulate the flow. In Fig. 14, we plot the mean prediction from the ensemble of simulations (solid line) along with the ± 3 standard deviation bounds (dashed lines). The experimental measurements are plotted as symbols. We also plot a horizontal line at $y/d_j = 3$. We only use the measurements above the horizontal line in our calibration study to remove any influence of the boundary layer on the JPDF of $\mathbf{C}$. We see that the dashed lines do bracket the experimental data, except for about 10 probes in the last station of probes at $x/d_j = 42$. This shortcoming will necessarily impair the quality of the calibration. Note that the 10 probes are a small fraction of the 121 probes used in this studv.

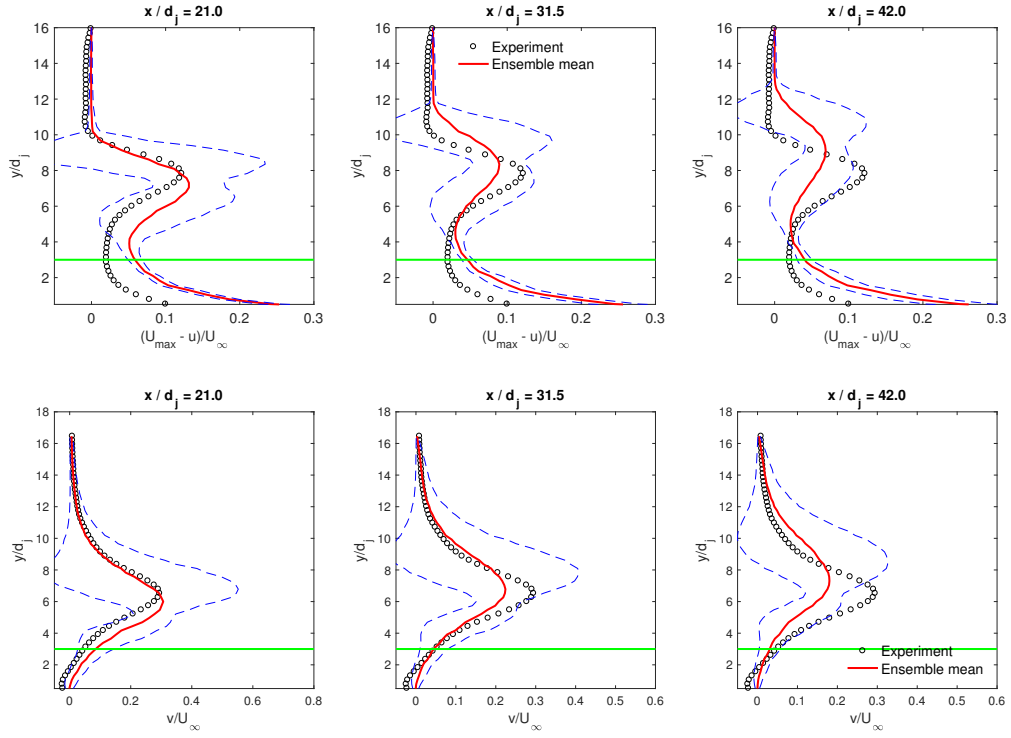

Fig. 14 Streamwise velocity deficit (above) and normalized vertical velocity (below) computed using 100 $\mathbf{C}_{nom}$ values sampled from the prior of the $(M = 0.8, J = 16.7)$ test case, at three streamwise locations $(x/d_j = 21, 31.5$ and $42.0)$. The symbols denote the experimental measurements. The solid line is the mean prediction of the ensemble of 100 simulations, and the dashed line are the $\pm 3\zeta$ bounds of the simulation, where ζ is the standard deviation of predictions.